SAPIENZA
UNIVERSITÀ DI ROMA

Department of
Civil, Constructional and Environmental Engineering
Geodesy and Geomatics Division

Ph.D. Course in Infrastructures and Transportations
XXV Ciclo

High resolution radargrammetry with COSMO-SkyMed, TerraSAR-X and RADARSAT-2 imagery: development and implementation of an image orientation model for Digital Surface Model generation

Candidate
Paola Capaldo

Supervisor
Prof. Mattia Crespi

Rome, 11 April , 2013

C'é un giorno per seminare e un giorno per raccogliere...
giovedí andrebbe benissimo.

Corrado Guzzanti,

Contents

List of Figures

List of Tables

Abstract

Digital Surface and Terrain Models (DSM/DTM) have large relevance in several territorial applications, such as topographic mapping, monitoring engineering, geology, security, land planning and management of Earth's resources. The satellite remote sensing data offer the opportunity to have continuous observation of Earth's surface for territorial application, with short acquisition and revisit times, satisfying the demand for monitoring rapid changes in the ground and anthropic activities. Meeting these requirements, the SAR (Synthetic Aperture Radar) high resolution satellite imagery could offer night-and-day and all-weather functionality (clouds, haze and rain penetration), that represents an important advantage for time-series analysis and for rapid mapping. This work is focused on the generation of radargrammetric DSM/DTM from high resolution SAR imagery and in detail, it is focused on the image orientation model for radargrammerty. Two different methods may be used in order to generate DSMs from SAR data: the interferometric and the radargrammetric approaches. The radargrammetry uses only the intensity information of the SAR images and reconstructs the 3D information starting from a couple of images similarly to photogrammetry. The interferometry uses the phase differences information between the SAR images to lead the terrain elevation. At present, it is pretty well known that the radar interferometry may suffer for lack of coherence, especially over areas with vegetation/forest. In this sense, radargrammetry could be a possible alternative solution to avoid the classical decorrelation problem affecting the interferometric technique, using just a couple of images with appropriate geometric configuration. Nowadays, the importance of the radargrammetric approach is rapidly growing due to the new high resolution imagery (up to 1 m of ground resolution) which can be acquired by COSMO-SkyMed (Italy), TerraSAR-X (Germany) and RADARSAT-2 (Canada) sensors in SpotLight mode. Radargrammetric DSM extraction procedure consists of two basic steps: the stereo pair orientation and the

image matching for the automatic detection of homologous points.

The goal of this work is the definition and the implementation of a geometric model in order to orientate SAR imagery in zero Doppler geometry. As regards the radargrammetric orientation model, it should be underlined that, starting from the model proposed in the classical book of Leberl (Radargrammetric image progessing), a refinement of the orbital model is needed to comply with and to exploit the potentialities of the novel high resolution (both in azimuth and in range). The radargrammetric model implemented in SISAR (Software per Immagini Satellitari ad Alta Risoluzione - developed at the Geodesy and Geomatic Division - University of Rome "La Sapienza") is based on the equation of radar target acquisition and zero Doppler focalization. The radargrammetry technique performs a 3D reconstruction based on the determination of the sensor-object stereo model, in which the position of each point on the object is computed as the intersection of two radar rays coming from different positions and therefore with two different look angles. Actually, these radar rays can be simply modeled as two segments of measured lengths centered in two different positions (along two different satellite orbits), so that the intersection generating each object point is one of the two possible intersections between two circumferences centered in the two different positions and laying into two planes orthogonal to the two different satellite orbits whose radii are equal to the segment measured lengths.

The crucial issue for the image orientation is the orbital estimation. Starting from a first orbital function, the satellite position estimation has been changed during the tests. Initially, for the short length of SpotLight orbit acquisition, the metadata state vector positions and times were used to estimate the parameters of simple circular orbit. This approximation needed a few number of Ground Control Points (GCPs) to correct some SAR acquisition parameters. Following, the orbit interpolation has been changed from a circumferences to a Lagrange polynomial. This polynomial allow the possibility to oriented a SAR stereo pairs without use GCPs. Moreover a tool for the SAR Rational Polynomial Coefficients (RPCs) generation has been implemented in SISAR software, similarly to the one already developed for the optical sensors. The Rational Polynomial Functions (RPFs) model with the employment of RPCs is a well known method to orientate optical satellite imagery. In fact some satellite imagery vendors have considered the use of RPF models as a standard to supply a re-parametrized form of the sensor model in term of the RPCs, secretly generated from their own physical sensor models. This generalized method is very simple, since its implementation is standard and unique for all the sensors; it relates the object point coordinates (latitude ϕ, longitude λ and height h) to the pixel coordinates (I, J) in the form of ratios of polynomial expressions, moreover the RPFs model orientation accuracy using the RPCs is at level of the geometric models ones. The possibility to generate SAR RPCs starting from a radargrammetric model sounds

of particular interest since, at present, the most part of SAR imagery is not supplied with RPCs, although the RPFs model is available in several commercial software. Only RADARSAT-2 data are supplied with vendors RPCs. The RPCs can be an useful tool in place of the geometric model in processes as the image orthorectification/geocoding or as the DSMs generation, since the RPFs model is very simple and fast to be applied. To test the effectiveness of the implemented RPCs generation tool and the SISAR radargrammetric orientation model the reference results were computed: the stereo pairs were orientated with the two model. The test were carried out on several test site using COSMO-SkyMed, TerraSAR-X and RADARSAT-2 data. Moreover, to evaluated the advantages and the different accuracy between the orientation models computed without GCPs and the orientation model with GCPs a Monte Carlo test was computed.

At last, to define the real effectiveness of radargrammetric technique for DSM extraction and to understand the radrgrammetric tool implemented in a commercial software PCI-Geomatica v. 2012 , the images acquired on Beauport test site were used for DSM extraction by OrthoEngine tool (PCI-Geomatica toll for satellite imagery processing). It is important underline that several test were computed. This tests were carried out under the supervision of Prof. Thierry Tountin at CCRS (Canada Centre of Remote Sensing) where the PCI-Geomatica orientation model was developed, in order to check the better parameters solution to extract radargrammetric DSMs.

In conclusion, the results obtained are representative of the geometric potentialities of SAR stereo pairs as regards 3D surface reconstruction. The orientation accuracy, evaluated in terms of RMSE Control Points (CPs) residuals, is around 4/5 m. The results show the good performance of the software, considering not excellent accuracy of the available CPs. The orientation model, implemented in SISAR, without use of GCPs gives good results as the application of RPCs model to SAR stereo pairs what proves the effectiveness of the RPCs generation tool implemented in SISAR. The OrthoEngine DSM extracted shown the advantages and potentiality of radargrammetric technique as alternative or complementary solution to the interferometric technique in order to generated digital model from SAR data.

Chapter 1

Introduction

The possibility of near-real-time 3D Earth surface mapping satellite remote sensing data enable the possibility of continuous observation of the Earth's surface, with short times of acquisitions and revisit. This can satisfy the demand for the monitoring of rapid changes on the ground and in anthropic activities. In this respect, the availability of new high-resolution SAR (Synthetic Aperture Radar) spaceborne sensors offers new interesting potential for generation of radargrammetric DSMs (Digital Surface Models). The technologies provides for low cost, fast data acquisition and processing, independence from logistic difficulties, night-and-day, and all-weather functionality. These features are of crucial importance for security, land planning and management of Earth's resources, timely monitoring and management of disasters and emergencies such as geo-hydrological instability or geological/geophysical hazards in addition to the topographic mapping and monitoring engineering.

SAR satellite represent an already available tool for GMES (Global Monitoring for Environment and Security), the European Programme for the establishment of a European capacity for Earth Observation, and for several objectives of Horizon 2020, the new framework programme for research and innovation in Europe starting on 2014.

Two different methods to extract absolute or relative elevation from SAR data are interferometry and radargrammetry, both using a couple of images of the same area acquired from two different points of view. The interferometry uses the phase differences information between the SAR images to lead the terrain elevation. The radargrammetry using only the intensity information of the SAR

images and reconstructs the 3D information starting from a couple of images similarly to photogrammetry.

Actually, due to the low resolution amplitude supplied by the spaceborne radar sensors available until now (at the level of tens of meters), usually the first approach has been used, being aware that the radar interferometry may suffer for lack of coherence.

In fact the radargrammetric approach was first used in the 1950s; then, as mentioned, it was less and less used, due to the quite low resolution in amplitude of radar image, if compared to their high resolution in phase [34]. Only in the last decade some researchers have investigated the DSMs generation from very high resolution SAR data, for instance Raggam et al. [27] studied the potentialities of TerraSAR-X, and Toutin and Chenier [35] studied the RADARSAT-2 ones.

At present, the importance of the radargrammetric approach is rapidly growing due to the new high resolution imagery (up to 1 m GSD) which can be acquired by COSMO-SkyMed, TerraSAR-X and RADARSAT-2 sensors in Spot-Light mode. In this sense, it seems useful to underline that the two approaches should be considered complementary, in order to obtain the best (accurate and complete) product.

Two steps are necessary for radargrammetric DSM extraction: the image orientation and the image matching (automatic detection of homologous points). The goal of this thesis work is the DSM extraction from SAR data using the radargrammetric approach, in particular the definition and the implementation of a geometric model to orientate SAR images.

It is well known that the optimum stereo imagery configuration for the radargrammetric application is when the target is observed in opposite-side view; however it causes large geometric and radiometric disparities, hindering the image matching. A good compromise is to use a same-side configuration stereo pair with a convenient base to height ratio, in order to increase the efficiency in the correlation image process [23].

As regards the radargrammetric orientation model, it has to be underlined that, starting from the model proposed in the classical book of Leberl [20] , a refinement of the orbital model have to be taken into account to comply with and to exploit the potentialities of the novel high resolution (both in azimuth and in range). Therefore, the defined and implemented model performs a 3D orientation based on two range and two zero Doppler equations performed without GCPs (Ground Control Points) using the only metadata information.

The model has been implemented in SISAR (Software per Immagini Satellitari ad Alta Risoluzione), a scientific software developed at the Geodesy and Geomatic Division - University of Rome “La Sapienza”. This software was at first devoted to the orientation of high resolution optical imagery [12], and in the last years it has been extended also to SAR imagery.

Moreover a tool for the SAR Rational Polynomial Coefficients (RPCs) generation has been implemented in SISAR software, similarly to the one already developed for the optical sensors [11].

The Rational Polynomial Functions (RPFs) model with the employment of RPCs is a well known method to orientate optical satellite imagery. In fact, some satellite imagery vendors have considered the use of RPFs models as a standard to supply a re-parametrized form of the rigorous sensor model in terms of the RPCs, that implicitly provide the interior and external sensor orientation. This generalized method is very simple, since its implementation is standard and unique for all the sensors; moreover the performances of the RPFs model using the RPCs can reach the level of the ones from rigorous models.

The possibility to generate RPCs starting from a rigorous model sounds of particular interest since, at present, the most part of SAR imagery is not supplied with RPCs (only in RADARSAT-2 metadata the RPCs are available), although the RPFs model is available in several commercial software. The RPCs can be an useful tool in place of the rigorous model in processes as the image orthorectification/geocoding or as the DSMs generation, since the RPFs model is very simple and fast to be applied.

Deeper investigations in the least squares RPCs estimation underlined that many RPCs are correlated; so, in our approach the Singular Value Decomposition (SVD) and QR decomposition are employed to evaluate the actual rank of the design matrix and to select the actual estimable coefficients, avoiding an overparametrization of the model.

The results concern the stereo orientation using both the radargrammetric and the RPCs model. Moreover, to evaluated the difference accuracy between the orientation model calculated without GCPs and the orientation model calculated with GCPs a Monte Carlo test was computed.

In this thesis several tests were performed on SpotLight COSMO-SkyMed and high resolution SpotLight TerraSAR-X stereo pairs; the data available are a COSMO-SkyMed same-side stereo pairs, acquired over the areas of Merano (Northern Italy) and a opposite side stereo pair acquired on San Pietro island (Sardegna) and three TerraSAR-X images, acquired over the area of Hannover (Northern Germany), from which a same-side and an opposite-side stereo pairs have been derived, and on Trento test site two same side images.

In the area test of Beauport (Canada) we have three stereo pairs acquired by COSMO-SkyMed, TerraSAR-X and RADARSAT-2. The results are compared to those stemming from commercial software PCI Geomatica v. 2012, where the well known Toutin's model is implemented. Moreover, several DSMs were extracted using PCI-Geomatica to test the radargrammetry potentialities, under the supervision of Prof. Thierry Toutin, in order to check the better parameters solution to extract radargrammetric DSMs.

Chapter 2

Synthetic Aperture Radar

Rapid changes in the ground and anthropic activities require the acquisition of information in the shortest time and in the cheapest way; for this reason the studies about the potentialities of satellite imagery developed very fast in the last years. With the advent of instruments that produce images from electromagnetic radiation beyond wave-lengths to which the human eye and cameras are responsive, human vision and perception has been greatly extended. Remote sensing has evolved into an important supplement to ground observation ad aerial images in the study of terrain features, such as ground elevation. Due to high spatial resolution of civilian satellite Synthetic Aperture Radar (SAR) sensor since 1980s with the Shuttle Imagining Radar (SIR) a large number of researches around the world have investigated the elevation modelling and the production of Digital Elevation Models. In comparison with the aerial photogrammetric survey, the SAR satellite remote sensing offers some advantages:

- **easy monitoring of wide areas**
- **survey at regular interval:** depending only on satellite revisit time (variable from 1 day to few tens of days)
- **survey of areas logistically critical:** from the logistic point of view, where the organization of photogrammetric flights is difficult
- **possibility of night acquisition, acquisition in presence of clouds:**

This advantage is especially important for the medium scale cartography in developing countries or in countries with difficult political situations. So, the SAR

geomatics applications can be classified in the following categories: topographic mapping, deformation mapping, thematic mapping based on change detection, thematic mapping based on classification.

Moreover, SAR imagery are suitable for the DSM generation using radargrammetric or, more commonly, interferometric methods; to this aim, special mission have been set up, as the Shuttle Radar Topography Mission (SRTM), specially designed to yield elevation data on world scale, or ERS-1/2 tandem mission, or TanDEM-X mission in the last years.

2.1 Orbit feature

The target of satellite mission is to acquire the largest number of images with the best quality and the best areal coverage; in fact, the satellite orbit is determined by the combination of these requisites and by the revisit time and the distance Earth-satellite.

The orbit is planned considering the fact that the satellite has to observe the widest possible area of the Earth for a reasonable number of repetitions.

The preferred orbits for the Earth observation are usually Low Earth Orbits (LEO) with an altitude between 300 km and 1000 km. This choice represents a compromise between the necessity of a close observation of the Earth and the lifetime of the satellite; in fact the low orbit improves the resolution of images but produces negative effects such as atmospheric drag and gravitational perturbation which are the causes of the satellite lifetime reduction.

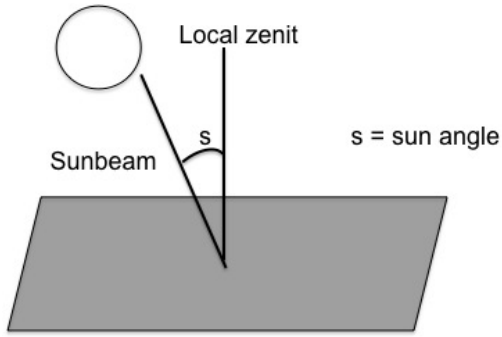

Figure 2.1: Sun angle

Also, the light condition, which is a crucial factor for the acquisition of optical imagery, is fundamental in the choice of the orbit.

The sun angle is the angle between the local zenith and the direction of sunbeam; it defines the light condition (Figure 2.1). The best light condition is

obtained with a less sun angle (sun at zenith), but presence of little shades could help the observer to recognize details and for a better interpretation of image. For this reasons sun angle usually can changes from 20° to 40°.

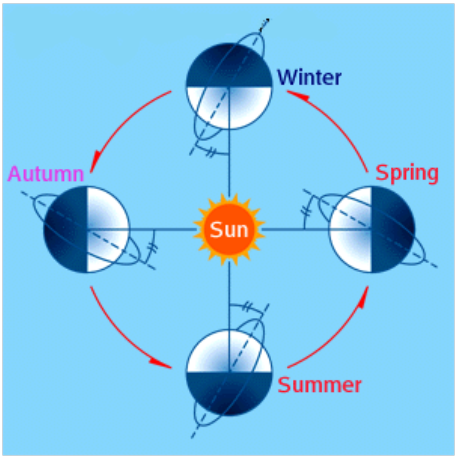

Figure 2.2: Sun-synchronous orbit

To guarantee the same lighting at each satellite passage, a Sun-Synchronous Orbit (SSO) is used (Figure 2.2). In this orbit the angle between Earth-Sun direction and the orbit plane is constant and the satellite flies over a certain area at the same local time therefore under the same conditions of light. The weather situations, such as mist, fog and clouds, are obviously unknown and are serious problem for the image acquisition. Obviously, this condition is important only in the case of optical images.

The inclination of the orbit - the angle between the orbital and the equatorial planes - is another relevant parameter to determine the satellite orbit (Figure 2.3). Orbits with large inclination - like pseudo-polar orbits - permit a total coverage of the Earth with only a very slight loss of data on the poles, whereas small inclinations are better in case of specific studies, for example on equatorial area. A good coverage depends not only on the orbit choice but also on the coverage of receiving stations, and on satellite revisit period.

The revisit period is the time between two consecutive acquisitions of the same area; for a satellite sensor it is usually of several days. In order to guarantee very short revisit period, satellite constellations have been launched on orbit, as Cosmo-SkyMED, TerraSAR-X and TanDEM-X, or Pleiades.

Actually, the majority of satellites offer overlap between contiguous orbits and for this reason some areas of the Earth can be acquired more frequently.

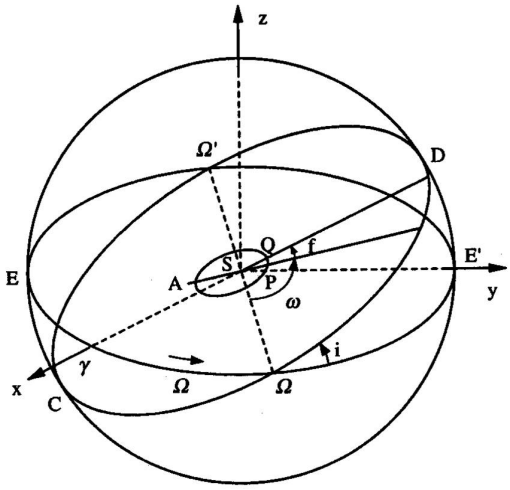

Figure 2.3: Orbit inclination

Some satellites are able to orient their sensors to shoot the same area in different passages, with shorter time intervals. The revisit period depends also on the inclination of the orbit and it is shorter if the inclination is smaller: this is the main disadvantage of the polar orbits [25].

2.2 Synthetic Aperture Radar

Radar is the commonly used acronym for Radio Detection and Ranging. Radio waves are that part of the electromagnetic spectrum that have wavelengths considerably longer than visible light, as shown in figure 2.4 below.

Imaging radar is an active illumination system, in contrast to passive optical imaging systems that require the Sun's illumination. An antenna, mounted on an aircraft or spacecraft, transmits a radar signal in a side-looking direction (right or left Fig. 2.5) towards the earth's surface.

The reflected signal, known as the echo, is backscattered from the surface and received a fraction of a second later at the same antenna, as shown in figure 2.6 below. The brightness, or amplitude (A), of this received echo is measured and recorded and the data are then used to construct an image. For coherent Radar systems such as Synthetic Aperture Radar (SAR), the phase of the received echo is also measured and used to construct the image [6].

Synthetic Aperture Radar takes advantage of the Doppler history of the radar

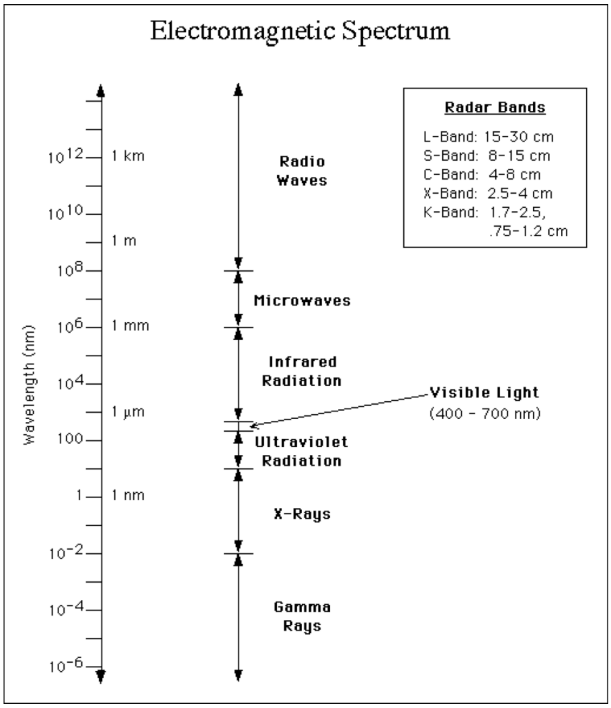

Figure 2.4: Electromagnetic Spectrum

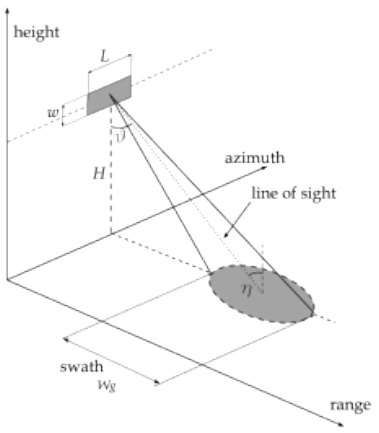

Figure 2.5: Side-looking configuration

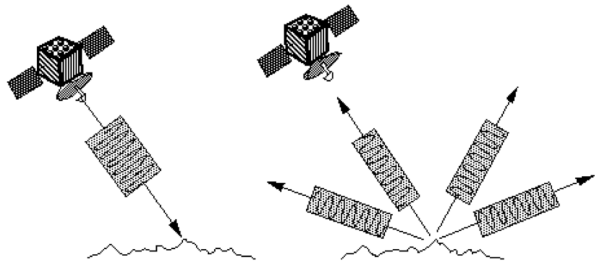

Figure 2.6: Echoes received back by antenna

echoes generated by the forward motion of the spacecraft to synthesise a large antenna, enabling high azimuthal resolution in the resulting image despite a physically small antenna, as shown is figure 2.7 . As the radar moves, a pulse is transmitted at each position. The return echoes pass through the receiver and are recorded in an echo store. Therefore, SAR system is based on the synthetic aperture principle, that simulates a longer antenna.

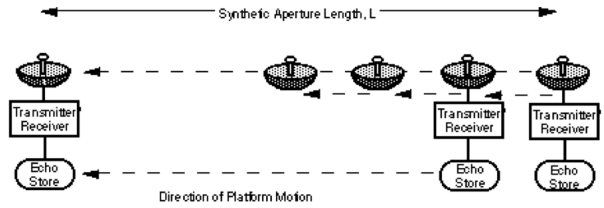

Figure 2.7: Constructing a synthetic antenna

SAR is a coherent, active, microwave imaging method that improves natural radar resolution by focusing the image through a process known as synthetic aperture processing.

Firstly, we can describe the received power P_r through the radar equation:

$$P_r = \frac{P_t G^2 \lambda^2}{(4\pi)^3 R^4} \sigma \tag{2.1}$$

where P_t is the transmitted power, G is the gain of the transmitted and received antenna, λ is the wavelength of the transmitted wave, R is the slant range, that represents the distance between the radar and the scene and σ is the radar cross section.

The received power depends on many parameters such as the frequency and polarization state of the emitted wave, the dielectric nature and the shape of the object and others. For example, buildings forming a corner with the ground or other buildings, correspond to high reflected energy. Conversely, roughness surfaces diffuse the incident energy and correspond to low reflected energy

The SAR satellite is an along-track sensor. It is made up of a linear detector array of CCDs (Charge Coupled Device) that obtains data in the platform's direction of motion (azimuth or along-track dimension). The sensor's instantaneous field of view extends the length of the swath width. The dimension parallel to the path of the platform carrying the sensor. The along-track dimension is the imaging direction of the sensor that is parallel to the direction in which the satellite or aircraft is moving . For side-looking radars, this dimension is sometimes called the range. The typical two-dimensional remotely sensed image is created by the movement of the platform in the along-track direction, while the sensor scans or aims at the orthogonal direction.

The dimension of the radar antenna determines the angular field of the signal beam in azimuth direction (ω_{h}) and in cross-track direction (ω_{v}) (see Figure 2.8); more exactly this angular values are dependent from the length (L) and from the width (w) of antenna respectively, as shown in the Equations 2.2.

$$\begin{aligned} \omega_h &= \frac{\lambda}{L} \\ \omega_v &= \frac{\lambda}{w} \end{aligned} \tag{2.2}$$

The swath extension can be approximately expressed by the following relation:

$$W_G \approx \frac{\lambda R_m}{w \cos \eta} \tag{2.3}$$

where λ is the wavelength of the microwave used, R_m is the slant range from the center of the antenna to the center of the footprint and η is the incident angle of radar beam pulse.

The resolution of a SAR image is defined by the resolution in azimuth (Δx) and in slant range direction (ΔR), or the ground resolution in cross-track direction (Δy).

The azimuth resolution, can be expressed by the Equation 2.4, according to the electromagnetic wave theory:

$$\Delta x = \frac{R\lambda}{L} \tag{2.4}$$

where R is the slant range, λ is the wavelength of the signal and L is the length of the antenna.

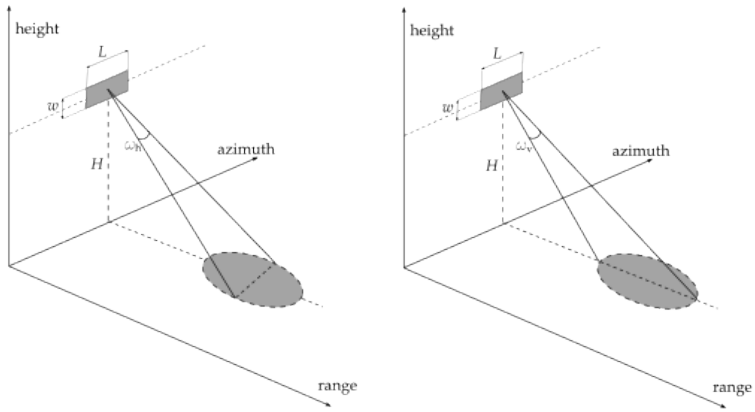

Figure 2.8: Angular field of signal in azimuth direction ω_{h} (left) and in cross-track direction ω_{v} (right)

The slant range and the ground range resolution can be expressed by the Equations 2.5 and 2.6:

$$\Delta R = \frac{c\tau_p}{2} \tag{2.5}$$

$$\Delta y = \frac{\Delta R}{\sin\vartheta} = \frac{c\tau_p}{2\sin\vartheta} \tag{2.6}$$

where c is the speed of light, τ_p is the pulse duration, and ϑ is the side-look angle.

The Equations 2.5 show that the slant range and the ground range resolutions are just dependent by the property of the signal, whereas the azimuth resolution is dependent by the position and size of antenna.

The Figure 2.9 shows the acquisition process of a SAR image along its synthetic aperture. The variation of the slant range R along the image acquisition causes the frequency shift of the echo backscattered from target, varying from an increase to a decrease.

So, considering the response of one point on the ground, the reflected signal from this point can be seen as a frequency modulated signal (Doppler frequency). Also, a filtering operation, called focusing, is applied along the azimuth axis under certain assumptions (width of Doppler spectrum and duration of the seen point), consequently the azimuth resolution Δx is improved as follows:

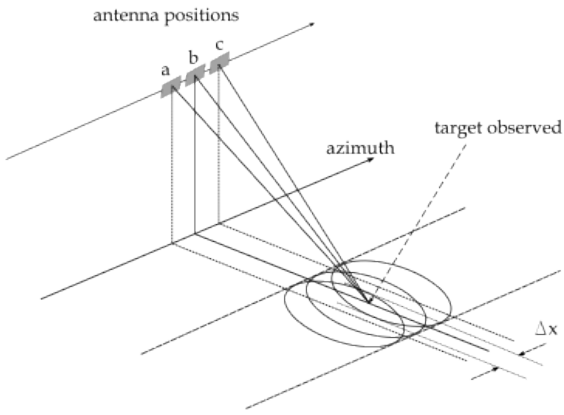

Figure 2.9: Imaging system of SAR

$$\Delta x = \frac{L}{2} \tag{2.7}$$

In this way the azimuth resolution is independent from the satellite position and it is related only to the size of antenna.

More generally, the direction of the radar pulse may be manipulated, obtaining a forward or a backward look of the radar beam. The beam is transmitted along a conical surface as shown in Figure 2.10. The axis of the cone is along the longitudinal axis of the antenna, and the squint angle τ steers the beam away from the zero Doppler direction, that is perpendicular to the flight path.

The center frequency of the passage of a point scatterer through the antenna beam is called the Doppler centroid frequency, f_{CD}, whereas zero Doppler, $f_D = 0$, denotes the direction in which the Doppler frequency is equal to zero, perpendicular to the flight direction.

The focused data of a satellite SAR image are "deskewed", that means to process the image such as the data are always observed effectively in zero Doppler geometry.

The time of the beginning of the recorded signal is called t_{start} and the end is referred t_{end}. Also, we can define the physical limit of the radar image which is processed in the slant plane (see Figure 2.11):

- the near range $R_{near} = (c \cdot t_{start})/2$
- the far range $R_{far} = (c \cdot t_{end})/2$

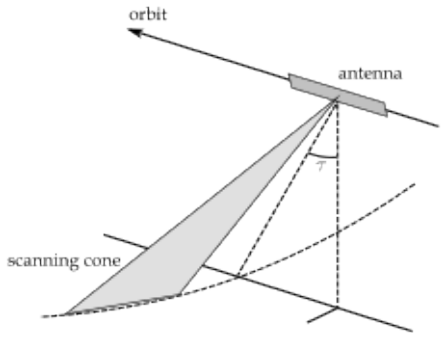

Figure 2.10: Definition of squint angle τ

Taking account for the post-processing aimed at the data focusing along the synthetic aperture, the SAR image generation is possible; in this way each pixel contains the information related to its position along the azimuth, to its slant range, to the amplitude of the signal backscattered and the phase information.

The field recorded at generic pixel x, denoted $E(x)$ can be written as:

$$E(x) = \sum_{s} a(s)\exp(i\psi(s))h(s,x) \tag{2.8}$$

where the summation ranges over the scatterers, $a(s)$ and $\psi(s)$ are respectively the amplitude and phase of the signal received from scatterer s, and h is the instrument function. The value of h is near 1 when s is in or near the resolving cell corresponding to pixel x, and near zero otherwise.

The detected field E is an array of complex numbers, that represents the image. The square of the modulus of the field at x is called the detected intensity; the square-root of the intensity is called the envelope or the amplitude. This is not the same as the amplitude of the received signal because the received field is perturbed by the instrument function. The amplitude of the received signal, $a(s)$, is called the reflectivity, and its square is called the surface cross-section. Unfortunately, this is contaminated with speckle noise [22].

As regards the swath extension and the operational modes, the SAR system can image an area over the ground in Stripmap mode or in spotlight mode.

In the well-known Stripmap mode, the radar antenna is pointed along a fixed direction with respect to the platform flight path and the antenna footprint covers

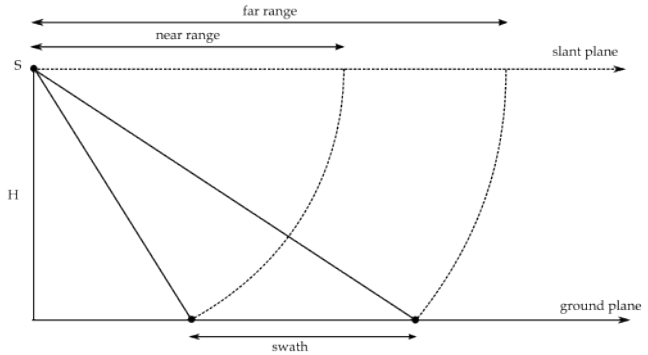

Figure 2.11: Slant range plane and ground plane projection

a strip on the imaged surface as the platform moves, see Figure 2.12. Accordingly, the extension of the illuminated area is theoretically unlimited in the azimuth direction, but the azimuth resolution cannot be better than a half of the real antenna azimuth length.

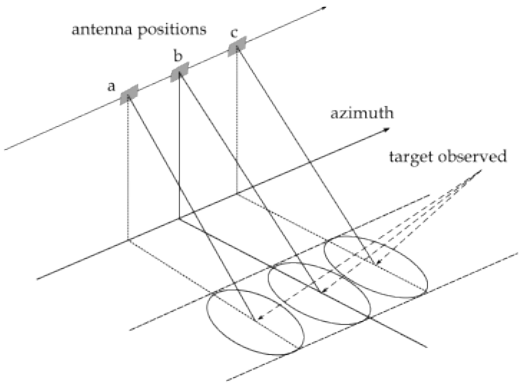

Figure 2.12: Stripmap acquisition mode

The spotlight configuration is used by the last generation satellite with high resolution, in fact in this acquisition mode the resolution in the azimuth direction is improved by increasing the synthetic aperture extension. The radar antenna beam is steered during the overall acquisition time, see Figure 2.13, thus pointing

always at the same area over the ground [19].

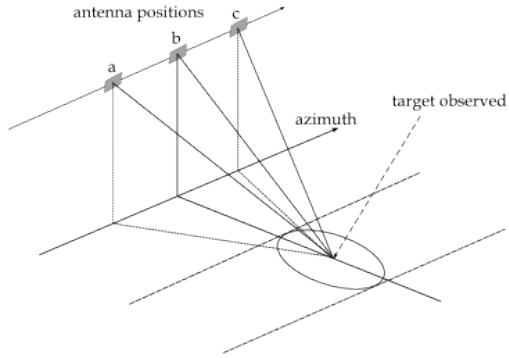

Figure 2.13: SpotLight acquisition mode

This configuration allows to obtain the best azimuth resolution to the detriment of the extension of the ground coverage [25].

2.3 SAR images distortions and peculiarity

One of the most readily apparent features of radar imagery is its sidelighted character, which arises through variations in the relative sensor to terrain geometry. Shadow areas and radar backscatter are affected by different surface properties over a range of incidence angles.

For flat terrain, the local reflection angle is the same as the incidence angle; most of the incident energy is reflected away from the sensor, resulting in a very low return signal. Rough surfaces, on the other hand, will scatter incidence energy in all directions and return a significant portion of the incident energy back to the antenna, as show in the scattering mechanisms figure below.

The shape and orientation of objects must be considered, as well as their surface roughness, when evaluating radar returns. For instance a particularly bright response will come from a corner reflector, which will produce a double bounce, as shown above. It is also worth noting that some features, such as corn fields, might appear rough when seen in both the visible and microwave portion of the spectrum, whereas other surfaces, such as roads, may appear rough in the visible range but look smooth in the microwave spectrum. In general, SAR images will manifest many more smooth, or specular, surfaces than those produced with optical sensors.

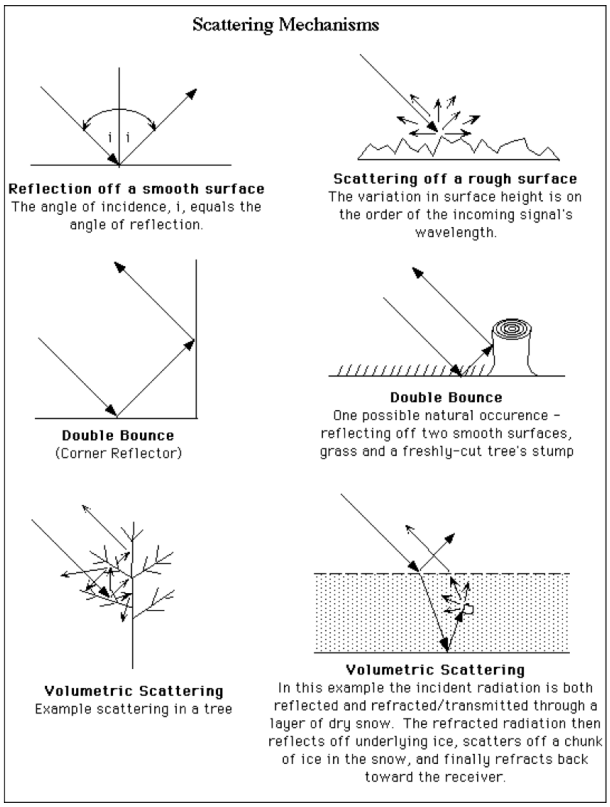

Figure 2.14: Scattering mechanism

2.3.1 Response of slope

An important SAR image acquisition characteristic is the direction of the displacement, that is directed toward the point of observation, whereas in classical aerial or satellite photogrammetry it is directed away from the nadir point. This deformation is typical in SAR geometry and causes the effects called foreshortening, layover and shadows. All these effects are quite important in order to understand at best a radar image, especially in mountainous areas.

The projection of a terrain slope according to SAR geometry induces well-known distortion, that in this section will be described.

In Figure 2.15 the distortion of the distance $\overline{AB}$ in ground and slant range projection is represented; the angle ACB, as defined with the auxiliary point C, is nearly equal to 90 degrees, therefore the relation between ground and slant

range distance reads:

$$d_s \cong d_g \sin \vartheta_B \tag{2.9}$$

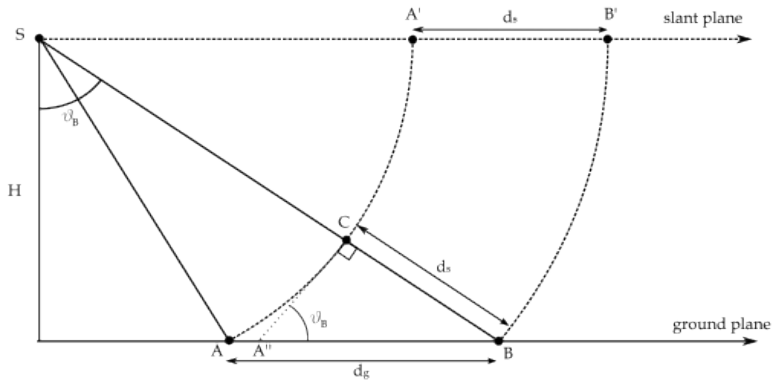

Figure 2.15: Distance $\overline{AB}$ in ground projection d_g and in slant range projection d_s

The smaller is the side-look angle, ϑ_B, to point B, the smaller is the distance in slant range projection, d_s, for a given ground distance d_g.

Now, the relief displacement on a SAR images is considered and described. Let us now consider a point A, that is situated on top of a vertical structure of height h.

From Figure 2.16 we can deduce that under the hypothesis of small height h in respect to the flying height H, the real relief displacement $A'B$ could be conveniently replaced by the displacement $A''B$, obtained through orthogonal projection. So, for a small height h, we can assume:

$$A'B \cong A''B \tag{2.10}$$

Under this assumption, it is possible to define simply the relief displacement in a SAR image.

In both ground and slant range projection, the relief displacement, p_g and p_s, is introduced. From Figure 2.17, using simple geometric relations, the form of the relief displacement in ground range projection reads:

$$p_g \cong h \cot \vartheta \tag{2.11}$$

The relief displacement in slant range projection reads:

$$p_s \cong h \cos \vartheta \tag{2.12}$$

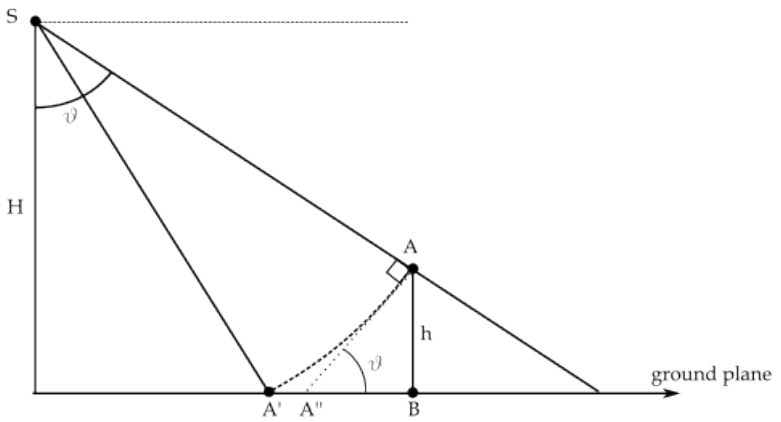

Figure 2.16: Simplifying assumption for relief displacement

The same height h produces a slightly smaller relief displacement in a slant range projection than it produces in a ground range presentation; this is the result of the overall compression of the image in a slant range projection, usual in a SAR image [25].

It is also obvious that the displacement increases with larger height h and with smaller side-look angles ϑ.

Foreshortening effect

The foreshortening occurs when a slope, having an aspect directed toward the satellite, is almost perpendicular the the line of sight; in this case the bottom and the top of the slope appear on the slant range projection closer than they are really (see Figure 2.18). This effect is maximum when the radar beam is perpendicular to the mountain slope (see Figure 2.18), where the slope might appear as a line in the image.

Layover effect

The layover occurs when a slope angle is greater than the side-look angle; in this case the signal reflected by the top of the slope is recorded before the signal reflected by the bottom (see Figure 2.18).

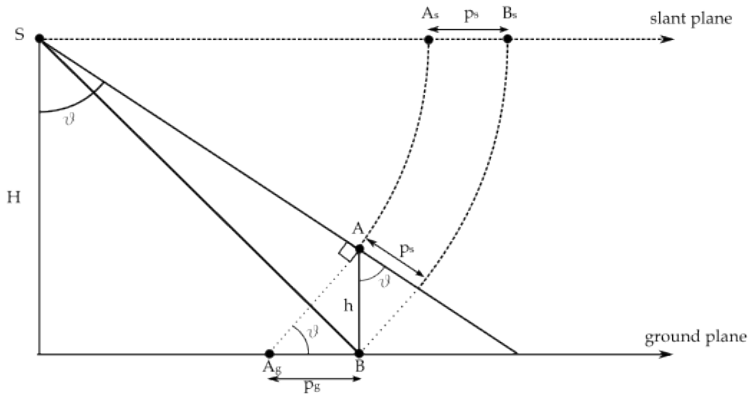

Figure 2.17: Relief displacement on a SAR image

Shadowing effect

The shadowing effect occurs when the radar beam is not able to illuminate the radar scene. This effect, that is shown in Figure 2.18, is considered as an optical shadow and induces a black area on the radar image because no reflected wave comes from this kind of region.

2.3.2 Response of soil

Because the dielectric constant for water is at least 10 times that for dry soil, the presence of water in the top few centimetres of bare, unvegetated soil can be detected in radar imagery, becoming particularly apparent at longer wavelengths.

2.3.3 Response of vegetation

A vegetation canopy will interact with radar waves as a group of volume scatterers, as shown in figure **??** above. The canopy is composed of a large number of discrete plant components, such as leaves, stems, stalks, limbs and so on. In addition, the canopy is underlain by soil that may result in surface scattering of the energy that penetrates the vegetation canopy. In general, shorter wavelengths, of approximately 2 to 6 cm, are best for sensing crop canopies and tree leaves, because at these wavelengths volume scattering predominates and surface scattering from the underlying soil is minimised. However, longer wavelengths, of approximately 10 to 30 cm are best for sensing tree trunks or limbs.

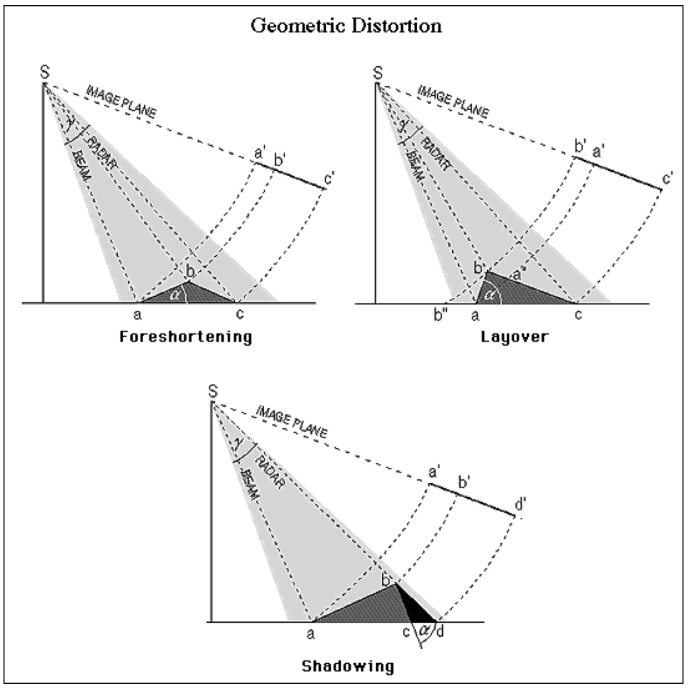

Figure 2.18: Foreshortening, Layover and Shadowing effects

2.3.4 Response of water and ice

Smooth water surfaces yield no returns to the antenna, but rough water surfaces return radar signals of varying strengths. In addition, waves moving in the range direction, that is moving toward or away from the radar system, are easier to detect that waves moving in the azimuthal direction.

Radar backscatter from sea ice is dependent on the dielectric properties and spatial distribution of the ice. Such factors as ice age, surface roughness, internal geometry, temperature, and snow cover will also all play a role in the affect of radar backscatter.

Each of these above topics are discussed in more detail in the sections within the handbook relating to these applications.

2.4 SAR satellite missions

2.4.1 COSMO-SkyMed

COSMO-SkyMed (COnstellation of small Satellites for Mediterranean basin Observation) is the largest Italian investment in Space Systems for Earth Observation, commissioned and funded by Italian Space Agency (ASI) and Italian Ministry of Defense (MoD), and it is natively conceived as a Dual-Use (Civilian and Defence) end-to-end Earth Observation System aimed to establish a global service supplying provision of data, products and services compliant with well-established international standards and relevant to a wide range of applications, such as Risk Management, Scientific and Commercial Applications and Defence/Intelligence Applications.

The system consists of a constellation of four Low Earth Orbit mid-sized satellites, each equipped with a multi-mode high-resolution Synthetic Aperture Radar (SAR) operating at X-band and fitted with particularly flexible and innovative data acquisition and transmission equipment.

The system is completed by dedicated full featured Ground infrastructures for managing the constellation and granting ad-hoc services for collection, archiving and distribution of acquired remote sensing data [3].

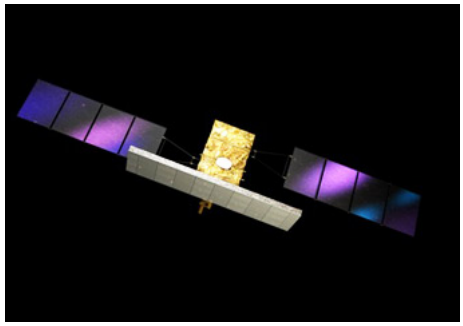

Figure 2.19: COSMO-SkyMed satellite

The fourth satellite has been launched on November 6, 2010; it is the last component of the mission, that is now finally fully operational.

The set of requirements, imposed at highest level, has brought to the following needed performances:

- large amount of daily acquired images
- satellites worldwide accessibility
- all weather and day/night acquisition capabilities

Radar sensor	X-band
Radar frequency	9.60 GHz
Resolution	1 m, 3 m,15 m o 30 m
Orbital altitude	619 km
Angle of inclination	97.86
Mission life time	at least 7 years

Table 2.1: COSMO-SkyMed sensor characteristics

- very fine image quality (e.g. spatial and radiometric resolution)
- possibility of image spatial resolution trade-off with size, at most possible extent and including sub-meter resolution

The sensor characteristics are summarized in the Table **??**. The Tandem interferometric configurations is supported, in which the two satellites fly in close proximity achieving the acquisitions with a temporal gap of 24 hours. In this case the coherence problem may be only attenuated but not totally solved as for the TerraSAR-X TanDEM mission (see section 2.4.2).

COSMO-SkyMed is able to operate in three different acquisition mode:

- **SpotLight Mode:** the antenna is steered during the acquisition time in order to illuminate the required scene for a time period longer than the one of the standard strip side view, increasing the length of the synthetic antenna and therefore the azimuth resolution (at expense of the azimuth coverage).

  The two different implementation allowed for this acquisition mode are SMART (only for defence purposes) and the Enhanced SpotLight.

  In Enhanced SpotLight the extension in azimuth direction is achieved by a antenna electronic steering scheme requiring the center of the beam steering to be located beyond the center of the imaged spot, thus increasing the observed Doppler bandwidth for each target.

  The extension of the frame is about 11 Km $\times$ 11 Km, in azimuth and range direction respectively, the ground resolution is about 1 m $\times$ 1 m.

- **Stripmap Mode:** it is the most common imaging mode, obtained by pointing the antenna along a fixed direction orthogonal to the orbit. The antenna footprint covers a strip on the illuminated surfaces as the platform moves and the system operates. The acquisition is virtually unlimited in

the azimuth direction, except for the limitations deriving from the SAR instrument duty cycle (about 600 s, allowing a strip length of 4500 km).

Two different implementation of this mode are provided: the Himage and the PingPong.

The Himage is characterized by a swath width of about 40 km and, an azimuth extension for the standard product (square frame) of about 40 Km (corresponding to an acquisition of about 6.5 s); ground resolution is about 3 m $\times$ 3 m.

In the PingPong mode the acquisition is performed in strip mode alternating the signal polarization between two of possible ones, i.e. VV, HH, HV and VH. In this polarimetric burst mode only a part of the synthetic antenna length is available in azimuth and consequently the azimuth resolution is reduced. This mode is characterized by a swath width value of about 30 km and an azimuth extension for the standard product of about 30 Km (square frame) corresponding to an acquisition of about 5.0 s; ground resolution is about 15 m $\times$ 15 m.

- **ScanSAR Mode:** it allows larger swath in range with respect to the Stripmap one, but with a less spatial resolution, obtained by periodically stepping the antenna beam to neighbouring sub-swaths. Since only a part of the synthetic antenna length is available in azimuth, the azimuth resolution is hence reduced. In such configuration the acquisition is performed in adjacent strip mode, hence it is virtually unlimited in the azimuth direction, actually it is about 600 s due to the limitations deriving from the SAR instrument duty cycle.

  The two different implementation are allowed for this acquisition mode are WideRegion and HugeRegion, with a spatial resolution selectable from 30 m $\times$ 30 m to 100 m $\times$ 100 m.

  In the WideRegion mode the swath extension in range direction is about 100 Km, corresponding to three adjacent subswaths. The azimuth extension for the standard product is about 100 Km (hence envisaged for the origination of a square frame) corresponding to an acquisition of about 15.0 s.

  In the HugeRegion mode the grouping acquisition over up to six adjacent subswaths allows achieving ground coverage of about 200 Km in the range direction. The azimuth extension for the standard product is about 200 Km (hence envisaged for the origination of a square frame) corresponding to an acquisition of about 30.0 s.

The COSMO-SkyMed products for civil users are divided in Standard and Higher level products [2].

The SAR Standard products are the basic image products of the system, classified in many levels of processing, coded as follows:

- **Level 0 RAW data:** this data consists of time ordered echo data, obtained after decryption and decompression and after applying internal calibration and error compensation; it includes all the auxiliary data required to produce the other basic and intermediate products
- **Level 1A, Single-look Complex Slant (SCS) product:** RAW data focused in slant range and zero Doppler projection, that is the sensor natural acquisition projection; product contains In-Phase and Quadrature of the focused data, weighted and radiometrically equalized
- **Level 1B, Detected Ground Multi-look (DGM) product:** obtained detecting, multi-looking and projecting the Single-look Complex Slant data onto a grid regular in ground (note that SpotLight Mode products are not multi-looked)
- **Level 1C/1D, Geocoded product GEC (1C Level product) and GTC (1D Level product:)** obtained projecting the 1A product onto a regular grid in a chosen cartographic reference system. In case of Lev 1C the surface is the Earth ellipsoid while for the Lev 1D a DEM (Digital Elevation Model) is used to approximate the real Earth surface. In Lev 1D data is constituted by the Backscattering coefficient of the observed scene, multi-looked (except for SpotLight Mode), including the annexed the Incidence Angles Mask

The SAR Higher Level products, suited for mid or even high level remote sensing applications, are composed by the following products:

- **Quicklook:** reduced spatial resolution image for browsing purposes
- **Co-registered products:** a set of image layers coregistered together (i.e. merged in vertical direction), for interferometry, change detection and so on
- **Mosaiked products:** a set of image joined together (i.e. merged in horizontal direction), for large spatial coverage representation
- **Speckle filtered image:** an image with an increased equivalent number of looks (ENL), obtained through various filters available (more details in [2])
- **Interferometric products:** interferometric coherence and phase, in support of the interferometric applications

- **DEM products:** digital elevation data and related height error map obtained with interferometric techniques

The data packaging organization adopted as distribution format for the civilian standard products is HDF5.

2.4.2 TerraSAR-X

TerraSAR-X is a commercial German synthetic aperture radar (SAR) Earth observation satellite which was launched in June 2007 with a scheduled lifetime of 5 years. The satellite design is based on well-founded technology and knowledge achieved during the successful Synthetic Aperture Radar SIR-C/X-SAR and SRTM missions. It carries a high frequency X-band SAR sensor which can be operated in flexible imaging modes in order to meet the requirements of versatile applications.

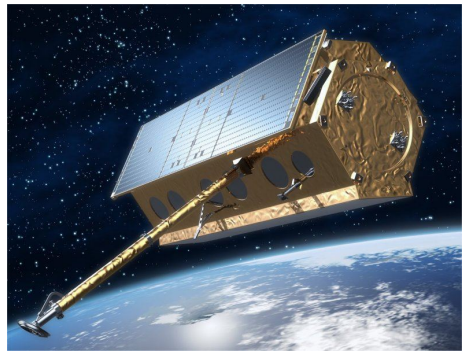

Figure 2.20: TerraSAR-X satellite

The TerraSAR-X mission is a Public Private Partnership (PPP) between the German Ministry of Education and Science (BMBF) represented through the German Aerospace Centre (DLR) and Europe's leading space company, EADS Astrium GmbH. Astrium successfully developed, integrated, and tested the satellite. Commercial distribution of TerraSAR-X data, value-adding, service development, and user training are the tasks of Infoterra GmbH, a 100ground segment for reception, processing, archiving and distribution of the X-band SAR data. DLR is also responsible for instrument calibration, the 5 years of operation and the scientific distibution of TerraSAR-X data within the TerraSAR-X science team.

It carries a high frequency X-band SAR sensor which can be operated in flexible imaging modes in order to meet the requirements of versatile applications.

Radar sensor	X-band
Radar frequency	9.65 GHz
Resolution	1 m, 3 m,16 m
Orbital altitude	514 km
Angle of inclination	97.4
Mission life time	at least 5 years

Table 2.2: TerraSAR-X sensor characteristics

It is very similar to its Italian competitor COSMO-SkyMed, without offering a satellite constellation however, and it can acquire imagery in several operational mode:

- **SpotLight (SL):** it an imaging modes that use phased array beam steering in azimuth direction to increase the illumination time, i.e. the size of the synthetic aperture. This leads to a restriction in the image/scene size. Two kinds of scene size are available: 10 km × 10 km for the SpotLight mode with 2 m resolution and 10 km × 5 km (width × length) in the HighResolution SpotLight (HS) mode with 1 m resolution.

- **StripMap (SM):** it is the basic SAR imaging mode, in which the ground swath is illuminated with continuous sequence of pulses while the antenna beam is fixed in elevation and azimuth. This results in an image strip with a continuous image quality (in flight direction).

  In StripMap mode, a spatial resolution of up to 3 m can be achieved. The standard scene size is 30 km × 50 m in order to obtain manageable image files; however, acquisition length is extendable up to 1,650 km.

- **ScanSAR (SC):** in this acquisition mode, electronic antenna elevation steering is used to acquire adjacent, slightly overlapping coverages with different incidence angles that are processed into one scene. In ScanSAR mode, a swath width of 100 km (and even more) will be achieved by scanning four adjacent ground sub-swaths with quasi-simultaneous beams, each with different incidence angle. Due to the switching between the beams, only bursts of SAR echoes are received, resulting in a reduced bandwidth and hence, reduced azimuth resolution.

  In the ScanSAR mode a spatial resolution of up to 18 m is achieved. The standard scene size is 100 km × 150 km (width × length) for easily manageable image files, but again, the acquisition length is extendable up to 1,650 km.

Moreover TerraSAR-X can operate in "Standard TerraSAR-X operational mode", with a single receive antenna mode, that uses a chirp bandwidth of up to 300 MHz, and in "Advanced imaging mode", where a dual receive antenna is used.

The Basic Image Products of TerraSAR-X are [4]:

- **Slant Range Product in SSC:** The slant range product is a single-look product of the focused radar signal in Single Look Slant Range Complex (SSC). The pixels are spaced equidistant in azimuth (according to the pulse repetition interval PRI=1/PRF) and in slant range (according to the range sampling frequency).

  The data are represented as complex numbers containing amplitude and phase information. Each image pixel is processed to zero Doppler coordinates in range direction, i.e. perpendicular to the flight track.

- **Multi-look Ground Range Detected - MGD:** This product is a detected multi look product with reduced speckle and approximately square resolution cells, with reduced spatial resolution. The image coordinates are oriented along flight direction and along ground range. The pixel spacing is equidistant in azimuth and in ground range.

- **Geocoded Ellipsoid Corrected - GEC:** The GEC is a multi-look detected product, which is resampled and projected to the WGS84 reference ellipsoid assuming one average height. The image is represented in map geometry with ellipsoidal corrections only, thus no terrain correction is performed. Available grid formats are UTM (Universal Transversal Mercator) and UPS (Universal Polar Stereographic). Since the ellipsoid correction does not use height information from a Digital Elevation Model (DEM) for geometric correction, the pixel location accuracy varies depending on the local terrain.

- **Enhanced Ellipsoid Corrected - EEC:** The EEC is a multi-look detected product as well, projected and resampled to the WGS84 reference ellipsoid. However, image distortions caused by varying terrain height are corrected using an external Digital Elevation Model (DEM) available at the payload ground segment (PGS), as SRTM global DSM [4]. The image is represented in map geometry with terrain correction. The available map projections are UTM or UPS. The pixel localization of this product is of a higher accuracy, however, it depends on the type of terrain, the quality and the resolution of the DEM used for the orthorectification, and the incidence angle of the acquisition.

As Enhanced Image Products TerraSAR-X offers:

- **Orthorectified Image - ORISAR:** a highly accurate geocoded image with terrain correction included

- **Radiometrically Corrected Image - RaNSAR:** the products has an additional radiometric calibration or radiometric normalisation

- **Mosaic - MCSAR:** in order to cover a geographical area larger than a standard scene, neighbouring geocoded or orthorectified images are combined into one image in a seamless way

- **Ascending/Descending Merge - ADMSAR:** the ADMSAR product is an orbit merge, i.e. a combination of SAR images from ascending and descending right looking orbits is used for image analysis

In June 2010 a "twin" of TerraSAR-x was launched, the satellite TanDEM-X (TerraSAR-X Add-On for Digital Elevation Measurement). It is a radar satellite almost identical to TerraSAR-X, that circles the Earth together with TerraSAR-X as a unique satellite formation.

They are at only a few hundred meters and they record data synchronously in the so-called StripMap Mode (3 m ground resolution) and thus acquire the data basis for a intereferometric global Digital Elevation Model (DEM) of an unprecedented quality, accuracy, and coverage, since coherence problems are totally solved by the almost contemporary acquisition of the two images used to form the interferogram.

The goal of this mission is to have a homogeneous elevation model available for the Earth's complete land surface in 2014. The expected vertical accuracy is of 2 m (relative) and 10 m (absolute), within a horizontal raster of approximately 12 m $\times$ 12 m, slightly varying depending on the geographic latitude.

2.4.3 RADARSAT-2

Launched in December 2007, Canada's next-generation commercial radar satellite offers powerful technical advancements that will enhance marine surveillance, ice monitoring, disaster management, environmental monitoring, resource management and mapping in Canada and around the world.

This project represents a unique collaboration between government and industry. MacDonald, Dettwiler and Associates Ltd. (MDA) will own and operate the satellite and ground segment. The Canadian Space Agency helps fund the construction and launch of the satellite and will recover this investment through the supply of RADARSAT-2 data to the Government of Canada during the lifetime of the mission.

Figure 2.21: Rasarsat-2 satellite

Radar sensor	C-band
Radar frequency	5.404 GHz
Resolution	1 m, 3 m,9 m
Orbital altitude	798 km
Angle of inclination	98.6
Mission life time	at least 5 years

Table 2.3: RADARSAT-2 sensor characteristics

This is achieved by leveraging the knowledge and experience gained through the long and successful RADARSAT-1 mission while taking advantage of new technologies.

A key priority of the Canadian Space Program is responding to the twin challenges of monitoring the environment and managing natural resources. The hardy, versatile RADARSAT Earth Observation satellites are a major data source for commercial applications and remote sensing science.

RADARSAT products also provide valuable information for major application areas in coastal and marine surveillance, and security and foreign policy [1].

It carries a high frequency C-band SAR sensor which can be operated in flexible imaging modes in order to meet the requirements of versatile applications.

- **High-resolution images:** The Ultra-Fine resolution mode, available on RADARSAT-2, acquires images at a spatial resolution of three metres. In this mode, the radar operates with the highest sampling rate, therefore the ground coverage is limited (10 to 30 km) to keep the acquisition within the recording limits. The Ultra-Fine imaging mode provides the one of the

best resolution available commercially with a spaceborne SAR system. This better detect targets that are closely spaced and provide enhanced definition of other targets, thereby reducing ambiguities and increasing confidence in the data.

- **Data polarization:** RADARSAT-1 provided horizontal transmit and horizontal receive (HH) data only. RADARSAT-2 can transmit horizontal (H) and vertical (V) polarizations and, depending on the selected mode, the sensor receives either H or V signals or both of the signals simultaneously. Therefore, in addition to providing complete RADARSAT-1 continuity, RADARSAT-2 generates products with VV polarization, cross-polarization (HV or VH), dual-polarization (HH+HV or VV+VH) or quad-polarization (HH+VV+HV+VH) over a range of spatial resolutions. This allows the end-user to select the combination that is best for the specific application.

  Each scattering element (HH, VV, HV and VH) has varying sensitivities to different surface characteristics and properties, helping to improve the discrimination between features. Moreover, polarimetric data can be used to characterize the polarimetric signature of various surface features, which is very useful in the study of scattering mechanisms and in resolving ambiguities about the observed area.

- **Dual-sided imaging:** RADARSAT-1 has wide area coverage with its large accessibility swath. However, the revisit time for some latitudes can be a limiting factor in some applications. Left- and right-looking modes on RADARSAT-2 reduce the revisit time by one half and the accessibility swath is doubled. In effect, the market for SAR images expands as applications that were not previously feasible will be given an opportunity to develop. Moreover, in emergency situations, the choice of beam mode and position can be set to ensure the greatest repeat coverage of the region of interest. Nominally, 10 minutes are required to switch from one side to the other. The flexibility of RADARSAT-2 makes it a powerful tool to support world mapping and disaster management activities.

RADARSAT-2 imaging modes

- **Fine beam modes:** Fine Beam modes are intended for applications which require higher spatial resolution and lower swath coverage. Fine Resolution Beams cover the incidence angle range from 30Â° to 50Â°. This imaging mode is available in co-polarization, cross-polarization, dual-polarization and quad-polarization.

  In addition, several new Fine Resolution products is available on RADARSAT-2, and the list of enhanced imaging modes follows.

- **Multi-look fine** The Multi-Look Fine Resolution Beam mode is the four-look version of the Fine Resolution mode, therefore providing the same spatial resolution with improved radiometric resolution. The four looks are made possible by the higher sampling rate of the RADARSAT-2 SAR. The Multi-Look Fine imaging mode is available in selective single polarization (HH or VV).

- **Ultra-fine beam** Ultra-Fine Beam modes of three-metre resolution is intended for applications which require very high spatial resolution. The Ultra-Fine Beam imaging mode is available in selective single polarization (HH or VV)

- **Standard beam modes** Standard Beams allow imaging over a wide range of incidence angles acquired in seven different modes referred to as S1 to S7. The incidence angles range from 20Â° at the inner edge of S1, to 49Â° at the outer edge of S7. Experience with RADARSAT-1 has demonstrated that the Standard Beam Mode generates image quality characteristics which provide a good compromise between spatial resolution, radiometric resolution and image coverage. On RADARSAT-2 this imaging mode is available in copolarization, cross-polarization, dual-polarization and quad-polarization.

Extended beam modes

- **Low incidence** An Extended Low Incidence Beam will cover the incidence angle range from 10Â° to 23Â° with a swath coverage of 170 km. At these incidence angles, the antenna operates beyond its optimum range, therefore some minor degradation of the image can be expected. The spatial resolution is the same as Standard Beams. This imaging mode is available in copolarization, cross-polarization and dual-polarization.

- **High incidence** The incidence angle range beyond 49Â° is covered with the High Incidence Beams up to 60Â°. As with the Low Incidence Beams, minor degradation of the image can be expected due the operation of the antenna outside its optimal range. The spatial resolution is the same as Standard Beams. This imaging mode is available in co-polarization, cross-polarization and dual-polarization.

- **Wide swath mode** Wide Swath Beams allow the coverage of a larger region than the Standard Beam at the expense of a slightly coarser spatial resolution. Three Wide Swath Beams cover a range on incidence angles from 20Â° to 45Â°. This imaging mode is available in copolarization, cross-polarization and dual-polarization.

- **ScanSAR mode** ScanSAR imagery is generated with a combination of single beams covering adjoining swaths. This provides the largest swath coverage available in RADARSAT-2 products. However, the increased coverage is obtained at the expense of spatial resolution. ScanSAR imaging mode is available in copolarization, cross-polarization and dual-polarization.

Chapter 3

Radargrammetry

3.1 Digital Elevation Model

Digital Elevation Model (DEM) is simply a statistical representation of the continuous surface of the ground by a large number of selected points with know X, Y, Z coordinates in an arbitrary coordinate field [13]. It is possible to distinguish between DSM (Digital Surface Models) and DTM (Digital Terrain Models

- the Digital Surface Model is the representation of the first reflective or visible surface, including trees, buildings, and any other features which is elevated above the ground;
- the Digital Terrain Model is the representation of the bare terrain, without any objects.

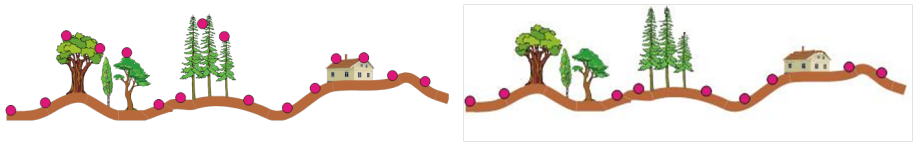

Figure 3.1: DSM and DEM

DEMs provide important knowledge of the area analyzed, therefore they are gaining growing relevance in several surveying applications:

- extracting terrain parameters;
- modeling water ow or mass movement (for example avalanches);
- rendering of 3D visualizations;
- creation of physical models (including raised-relief maps);
- rectification of aerial photography or satellite images;
- reduction (terrain correction) of gravity measurements (gravimetry,physical geodesy);
- terrain analyses in geomorphology and physical geography.

There are different methodologies to extract the digital elevation models: DEMs can be produced by automatic extraction from stereo satellite scenes ; they can be provided from Stereo Digital Aerial Photography at various resolutions; they can be generated by interpolating digital contour maps that may have been produced by direct survey of the land surface; they can be obtained by means of LIDAR (Laser Imaging Detection and Ranging) or using the Interferometric or Radargrammetric (procedure followed during the this) Synthetic Aperture Radar. Each of the listed techniques gives a different result in terms of accuracy and has advantages as well as disadvantages; hence the choice of the method depends on the requirements of the tasks to be accomplished.

The qualities of DEM products are assessed by how accurate the elevation is at each pixel, and how accurately the morphology is presented. Several factors are important to defne the quality of DEM-derived products:

- Terrain roughness;
- Sampling density (elevation data collection method);
- Grid resolution or pixel size
- Interpolation algorithm;
- Vertical resolution;
- Terrain analysis algorithm.

In the recent years, digital sensors carried on the spacecraft have enabled the generation of high resolution DEMs even over vast and hardly reachable areas, where the organization of tradition aerial photogrammetric flights results particular difficult and expensive.

3.2 Radrgrammetric approach

Radargrammetry is the technology of extracting geometric object information from SAR imagery.

Similarly to photogrammetry, radargrammetry forms a stereo model for 3D reconstruction.

Stereoscopic 3D reconstruction is an important process in the field of Computer Vision and refers to the ability to infer information on the 3D structure and distance of a scene, from a stereo pair of images . Stereo images are captured in the same way the human eyes capture scenes, and can provide depth information, just as human eyes provide perception about depth. While a 2D image provides only height and width, 3D reconstruction of the 2D image extends the information to a third dimension, depth. The major task of 3D reconstruction is to find the location of an object of interest in the left image and the location of that same object in the right image, with the objective of computing the disparity between the two objects, and eventually using this information to reconstruct the 3D scene. The 3D image reconstruction algorithms have been widely used in 3D imaging systems and to capture 3D surface information, as well as medical imaging [17].

The differences between images can be measured to establish a disparity map, that is used in radargrammetry to compute the terrain elevation from the measured parallaxes between the two images[36].

A simplified model is shown in Figure 3.2, where the area is flat, the flight lines are parallel and the height flight is constant; the Equation 3.1 is the relation for the height computation in case of slant-range projection, where h denotes the height of the scattered point, $p_{1,2}$ the absolute parallax and $\vartheta_{1,2}$ the incidence angles, the denominator sign "$\pm$" depends on the flight configuration, "$+$" for opposite-side and "$-$" for same-side stereo pair [14].

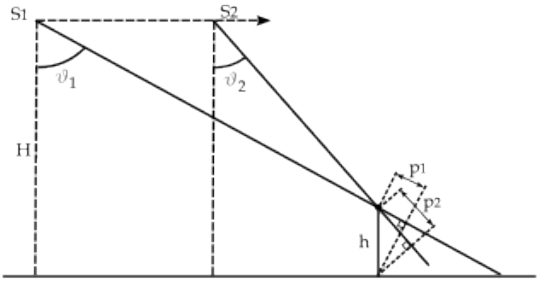

Figure 3.2: Terrain height computation using the parallaxes

$$h = (p_1 - p_2)/(\cos\vartheta_2 \pm \cos\vartheta_1) \tag{3.1}$$

In the 1960s, stereoscopic methods were first applied to radar images to derive ground elevation leading to the development of radargrammetry [26]. It was shown that some specific SAR stereo configurations would produce the same elevation parallaxes as those produced by aerial photos.

To obtain good stereo geometry, the optimum configuration for the radargrammetric application is when the target is observed in opposite-side view (see Figure 3.3); the intersection angle should be large in order to increase the parallax, that is to better determine the terrain elevation.

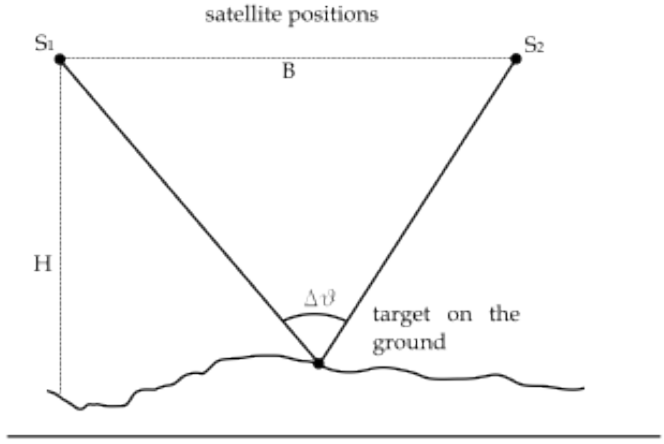

Figure 3.3: Stereo opposite-side for radargrammetry

Conversely, a small intersection angle implies a good stereo viewing, having a stereo-pair as nearly identical as possible.

The other fundamental step for the DSMs generation from SAR data using radargrammetry is in addition to the stereo model the image matching (paragraph 3.2.1). the automatic detection of homologous points. Opposite-side view, and large intersection angle cause large geometric and radiometric disparities hindering the image matching.

As mentioned, the DSM accuracy is strictly related to the matching process. In order to obtain good stereo geometry, the optimum configuration for the radargrammetric application is when the target is observed in opposite-side view; however it causes large geometric and radiometric disparities, hindering

image matching. A good compromise is to use a same-side configuration stereo pair with a base to height ratio ranging from 0.25 to 2 [23] in order to increase the efficiency in the matching procedure.

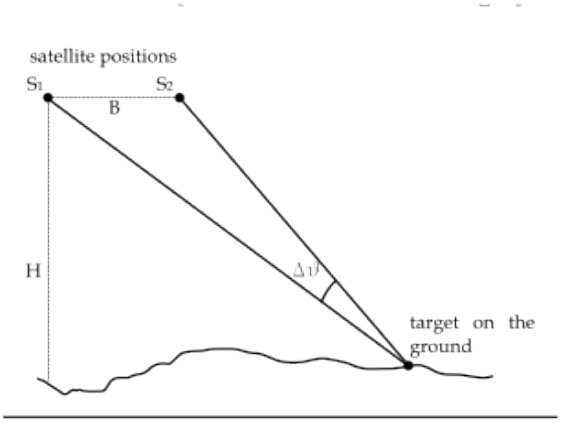

Figure 3.4: Stereo same-side configuration for radargrammetry

Only the amplitude information of a SAR images is used for radargrammetric measurement, whereas the interferometry uses the phase information.

An amplitude SAR image is similar to an optical image, obviously having different effects of distortion (see Paragraph 2.3). The gray tones of the image depend on several characteristics of the imaged surface, since the radar scene reflects a certain amount of radiation according to its geometrical and physical characteristics.

The electrical properties of the soil and the roughness of the area are crucial; moreover, as we have seen before, the geometric shape of an area or an object on the ground mainly determines the radiometry of a pixel and the brightness of a feature could be a combination with other objects. Another important parameter is the wavelength of the incident radiation wave and the electromagnetic interaction falls with either surface interaction or volume interaction (paragraph 2.3)[23].

Also, we can separate the interactions into two main topics:

- specular reflection: smooth surfaces that reflect all the incident waves; when the surface is tilted toward the radar the corresponding radar image appears very bright, conversely, if the surface is not turned toward the radar (e.g. calm water or paved roads), the surface appears dark on the radar image

- diffuse reflector: rough surface that scatters the incident wave in many directions

Also the side-look angle influences the signal reflection.

A typical phenomenon that occurs specially in urban area is the double bounce reflection, caused by the so-called corner reflector. This kind of object are characterized by two (or more) surfaces (generally smooth) forming a right angle, and are very common in urban areas. They appear as very clear targets on the radar image, indicated by a bright line, as shown in Figure 3.5, that represents an example of TerraSAR-X image in the urban area of Hannover (see paragraph 2.3) [37].

Figure 3.5: Double bounce effect in Hannover urban area, TerraSAR-X image

Usually, SAR imagery are affected by a high level of noise (speckle) due to the inherent nature of radar backscatter. The source of this noise is due to random interference between the coherent returns issued from the numerous scatterers present on the imaged surface, at the scale of the wavelength of the incident radar signal. Speckle noise gives the SAR image a grainy appearance and prevents target recognition and texture analysis efficiently. Therefore, an image preprocessing step to reduce speckle noise using several filters is required before starting the matching procedure ([15], [21], [30]).

As regards the radargrammteric model, figure 3.7 shows a general same-side configuration, in which the scene is observed from two different point of view with two different look angles.

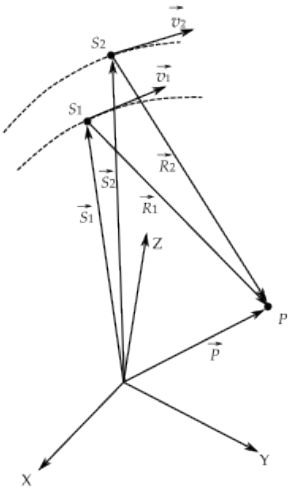

Figure 3.6: Basic stereo geometry for radargrammetry

Let S_1 and S_2 be the sensor positions, the object position P can be determined by the intersection of two radar rays with different look angles, leading a coplanarity condition expressed by:

$$\vec{S_1} + \vec{R_1} - \vec{S_2} - \vec{R_2} = 0 \tag{3.2}$$

where $\vec{S_1}$ and $\vec{S_2}$ denote the position vectors of sensors 1 and 2, while $\vec{R_1}$ and $\vec{R_2}$ denote the sensor-object vectors of two radar rays. The above conditions can be interpreted as the intersection of range spheres and Doppler cones, and thus we have two range equations and two Doppler equations given as follows:

Range equation:

$$\begin{aligned} \left|\vec{P} - \vec{S_1}\right| &= \left|\vec{R_1}\right| = R_1 \\ \left|\vec{P} - \vec{S_2}\right| &= \left|\vec{R_2}\right| = R_2 \end{aligned} \tag{3.3}$$

Doppler equation:

$$\begin{aligned} \vec{v_1}(\vec{P} - \vec{S_1}) &= 0 \\ \vec{v_2}(\vec{P} - \vec{S_2}) &= 0 \end{aligned} \tag{3.4}$$

where $\vec{v_1}$ and $\vec{v_2}$ denote the 3D velocity vectors of sensors 1 and 2. The equations 3.3 and 3.4 represent the general case of zero Doppler projection .

These four equations represent the base for the stereo model of radargrammetry; further details will be discussed in Chapter 4.

3.2.1 Image matching

As mentioned the image matching is the automatic detection of homologous points. Many different approaches for image matching have been developed in recent years. The main step of image matching process is to define the matching entity, that is a primitive (in the master image) to be compared with a portion of other (slave) images, in order to identify correspondences among different images. According to the kind of matching primitives, we can distinguish two basic techniques, the already mentioned ABM (Area Based Matching) and the Feature Based Matching (FBM). In ABM method, a small image window composed of grey values represents the matching primitive and the principal methods to assess similarity are cross correlation and Least Squares Matching (LSM); on the other hand, FBM uses, as main class of matching, basic features that are typically the easily distinguishable primitives in the input images, like corners, edges, lines, etc [10].

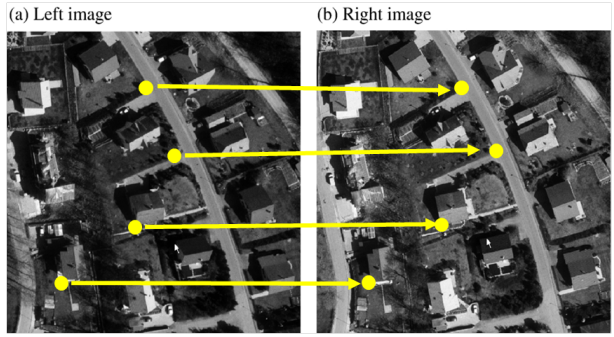

Figure 3.7: Homologous points

These strategies, if separately applied, do not appear suited to manage the strong geometrical deformation (like foreshortening and layover) and the complex and noisy radiometry (speckle) of SAR imagery.

Therefore, an original matching procedure has been developed. This matching method is based on a coarse-to-fine hierarchical solution with an effective combination of geometrical constrains and an ABM algorithm, following some ideas of [16] but with a complete original procedure and implementation. After image preprocessing, the two images are resampled reducing at each pyramid level the original resolution. The correspondences between points in the two re-

sampled images are computed by correlation. In this way the surface model is successively refined step by step, until the last step (corresponding to the original image resolution) where the final dense and accurate DSM is reconstructed. The advantage of this technique is that at lower resolution it is possible to detect larger structures, whereas at higher resolutions small details are progressively added to the already obtained coarser surface [24].

Chapter 4

SISAR Radargrammetric orientation model

4.1 Reference systems

In order to explain the orientation model implemented in SISAR, the definition of the used systems is necessary.

Earth-Centered Earth-Fixed system - ECEF (E): It is the standard global reference system, the origin is in the Earth center of mass, the X_E-axis is the intersection of equatorial plane and the plane of reference meridian (epoch 1984.0), the Z_E-axis is the mean rotational axis (epoch 1984.0) and the Y_E-axis completes the right-handed coordinate system (Fig. 4.1). [33], [38],

Image system (I): The image coordinate system is 2D and describes the position of a point in an image: the origin is in the upper left corner, the position is pointed out by its line (J) and sample (I); the line number increases downwards and the sample number increases toward the right. The line number J is related to the acquisition time, measured along the flying direction of the satellite (azimuth direction); the sample number I is related to the slant range of each point, that is the distance between the satellite and the imaged point on the ground (Fig. 4.2 a).

Correspondingly, as already underlined, the pixel dimension is characterized by two different resolutions: the azimuth resolution in flying direction (or line

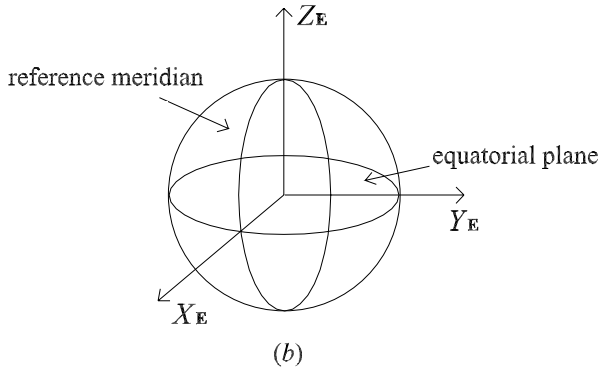

Figure 4.1: ECEF system

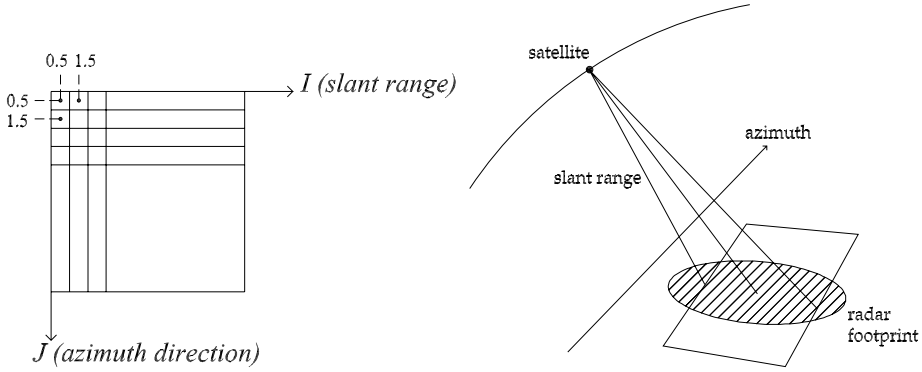

Figure 4.2: Image acquisition system (a) and azimuth and slant range direction in the image reference system (b)

spacing Δl) and the slant range resolution in the slant range direction (column spacing Δr)(Fig. 4.2b).

4.2 Classical projection equation

With the intent that introduce the Radargrammetric model implemented in SISAR, in the following paragraph the classical Leberl model will be explain. In figure 4.3, the satellite system and the object one are shown: $\underline{e_1}$, $\underline{e_2}$, $\underline{e_3}$ and $\underline{w}$,

$\underline{u}$, $\underline{v}$ are the unit vector of Cartesian axis of object (X,Y,Z) and satellite system respectively [20].

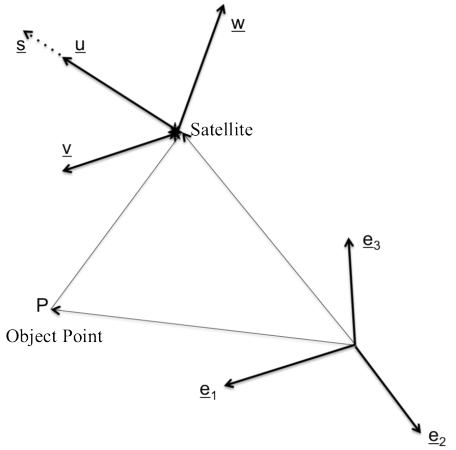

Figure 4.3: Definition of object space and sensor coordinate systems

The sensor position is (Fig.4.3):

$$S(t) = [X_S(t), Y_S(t), Z_S(t)]^T \tag{4.1}$$

and the antenna attitude with $\phi(t), \omega(t), \kappa(t)$. In the synthetic aperture radar, the synthetic antenna's velocity vector is the first derivate of position:

$$\dot{S}(t) = \left[\dot{X_S}(t), \dot{Y_S}(t), \dot{Z_S}(t)\right]^T \tag{4.2}$$

The position vector $\bar{P}$ of the object point P:

$$\bar{P} = X_P \cdot e_1 + X_P \cdot e_2 + Z_P \cdot e_3 \tag{4.3}$$

and in the sensor system

$$\bar{P}^* = u_P \cdot u + v_P \cdot v + w_P \cdot w \tag{4.4}$$

The Radar acquisition geometry is defined in figure 4.4 and the coefficients u_P, v_P, w_P are:

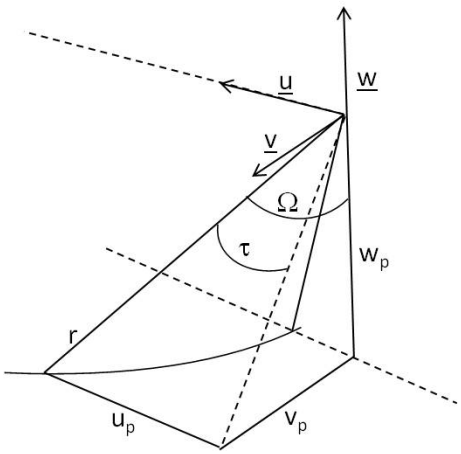

Figure 4.4: Relating squint angle, slant range, and elevation angle to sensor coordinates

$$
\begin{aligned}
u_P &= r_S \cdot sin\tau \\
v_P &= r_S \cdot (sin^2\Omega - sin^2\tau)^{1/2} \\
w_P &= -r_S \cdot cos\Omega
\end{aligned}
\tag{4.5}
$$

A rotation matrix A rotates the sensor system in the object system (u,v,w $\rightarrow$ e_1, e_2, e_3). In the zero Doppler acquisition geometry τ is equal to zero, since the target is acquired perpendicularly the satellite orbit direction

$$
\bar{P} = S + A \cdot \bar{P}^* \tag{4.6}
$$

Where:

$$
A = \begin{bmatrix} u_x(t) & u_y(t) & u_z(t) \\ v_x(t) & v_y(t) & v_z(t) \\ w_x(t) & w_y(t) & w_z(t) \end{bmatrix} \tag{4.7}
$$

and

$$
\begin{aligned}
\hat{u} &= (u_x, u_y, u_z) = \vec{\dot{S}}/|\vec{\dot{S}}| \\
\hat{v} &= (v_x, v_y, v_z) = (\vec{S} \times \vec{\dot{S}})/|\vec{S} \times \vec{\dot{S}}| \\
\hat{w} &= (w_x, w_y, w_z) = (\hat{u} \times \hat{v})/|\hat{u} \times \hat{v}|
\end{aligned}
\tag{4.8}
$$

If A(t) and S(t) are known functions of time, anyway for each point we have three equation (4.6) and four (P_X, P_Y, P_Z and Ω) or two equations and three unknowns: eliminating the elevation angle (angle between nadir and line of sight).

So we have a simple geometric description of radar case (Fig. 4.4)

$$\bar{P}^* = A^{-1} \cdot (\bar{P} - S) \tag{4.9}$$

$$\frac{u_P}{[v_P^2 + w_P^2]^{1/2}} = \tan\tau(u_P^2 + v_P^2 + w_P^2)^{1/2} = r_S \tag{4.10}$$

from which we also obtained:

$$|P - S| = r_S \tag{4.11}$$

$$u \cdot (P - S) = sin\tau \cdot |u| \cdot |P - S| = sin\tau \cdot r_S \tag{4.12}$$

The geometric locus of point is the intersection of range sphere (4.11) with cone (4.12)

The squint angle τ, as mentioned, is equal to zero in case of zero Doppler geometry, in fact it depends by Doppler frequency f_D:

$$f_D = \frac{2}{\delta \cdot r_S} \cdot u \cdot (S - P) \tag{4.13}$$

where δ is the, so τ result:

$$\sin\tau = \frac{\delta \cdot f_D}{2} \tag{4.14}$$

4.3 Radargrammetric model

The radargrammetric model implemented in SISAR is based on the equation of Radar target acquisition and zero Doppler focalization. The radargrammetry technique performs a 3D reconstruction based on the determination of the sensor-object stereo model, in which the position of each point on the object is computed as the intersection of two radar rays coming from different positions and therefore with two different look angles.

Actually, these radar rays can be simply modeled as two segments of measured lengths centered in two different positions (along two different satellite orbits), so that the intersection generating each object point is one of the two possible intersections between two circumferences centered in the two different positions and laying into two planes orthogonal to the two different satellite orbits whose radii are equal to the segment measured lengths [9]. In zero Doppler geometry the target is acquired on a heading that is perpendicular to the flying direction of

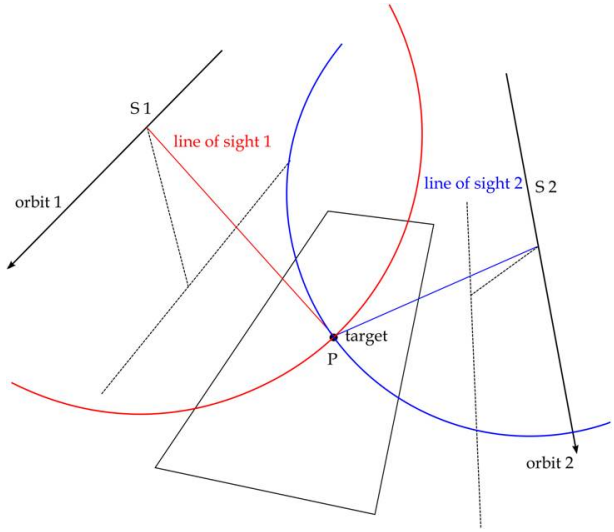

Figure 4.5: SAR acquisition system in zero Doppler geometry

satellite; the second equation is the slant range constrain. The couple of equations in a ECEF system reads:

$$\begin{cases} \sqrt{(X_P - X_S)^2 + (Y_P - Y_S)^2 + (Z_P - Z_S)^2} - (D_s + \Delta r \cdot I) = 0 \\ u_{S_X} \cdot (X_P - X_S) + u_{S_Y} \cdot (Y_P - Y_S) + u_{S_Z} \cdot (Z_P - Z_S) = 0 \end{cases} \tag{4.15}$$

where:

- X_P, Y_P, Z_P are the coordinates of the generic ground point P in the ECEF coordinate system
- X_S, Y_S, Z_S are the coordinates of the satellite in the ECEF coordinate system
- u_{X_S}, u_{Y_S}, u_{Z_S} are the Cartesian components of the satellite velocity in the ECEF coordinate system
- D_s is the so-called "near range"
- Δr is the slant range resolution or column spacing
- I is the column position of point P on the image

Moreover, the time of acquisition of each lines can be related to line number J through a linear function, since the satellite angular velocity can be considered constant along the short orbital arc related to the image acquisition

$$t = start\,time + 1/PRF \cdot J \tag{4.16}$$

The *start time* is the time of start of acquisition then the focalization processing, the inverse of *PRF* (Pulse Repetition Frequency),t is the time of each line acquisition and J the line number. The *start time*,*PRF* and *near range* are available in the metadata file of COSMO-SkyMed, TerraSAR-X and RADARSAT-2 product. Moreovere, for the TerraSAR-X products, the *start time* and the *near range* correction are supplied.

4.3.1 Orbit computation

The first step for the image orientation is the orbital estimation. The goal is estimated the satellite position for each line number of images according zero Doppler geometry.

In the metadata file, available with SAR imagery, the ECEF position ad velocity of satellite related to the time are presented. The number of state vector depend on SAR sensors but always presented in regular time interval.

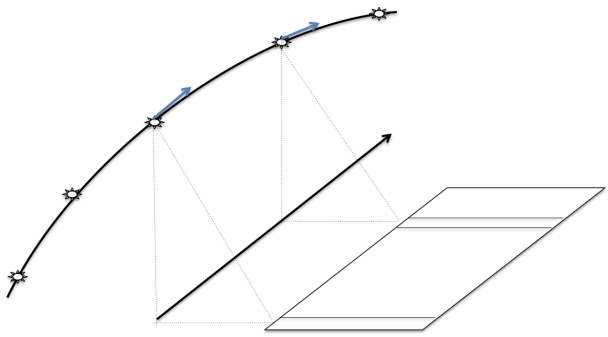

Figure 4.6: Orbit estimation

At first, for the short length of Spotlight orbit acquisition we used a simple function to interpolate the satellite flight path, a circumference. This kind of function need a few number of Ground Control Points (GCPs) (not less 3), points of which are know the image and ground coordinates, to estimate the parameters (4.16) *start time*, *PRF* and *near range* able to calculate the imagery orientation.

Subsequently, we change the orbit interpolation from a circumferences to a Lagrange polynomial (4.17). This kind of function don't require the conventional

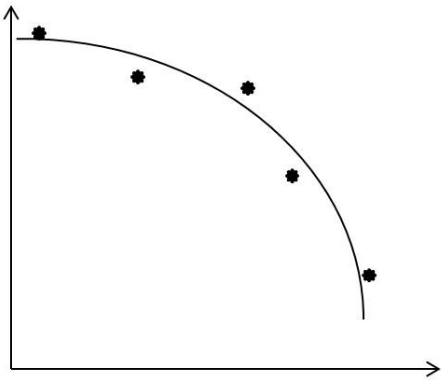

Figure 4.7: state vector positions

satellite orbit plane as inclination, right ascension, etc.

$$\begin{aligned} &L_k(x) = \prod_{i=0, i\neq k}^{N} \frac{x-x_i}{x_k-x_i} \quad k = 0, ..., N \\ &p_n(x) = y_0 \cdot L_0(x) + y_1 \cdot L_1(x) + ... + y_N \cdot L_N(x) = \sum_{k=1}^{N} y_k \cdot L_k(x) \end{aligned} \tag{4.17}$$

This function allows the possibility to use the metadata parameters (*start time*, *PRF*, *near range*) to estimate the images acquisition and the stereo orientation, without the use of GCPs. Polynomials parameters are estimated by Newton formula (4.18) using all orbital state vectors available in the ancillary data; this kind of rewritten Lagrange polynomial decrease the computational cost:

$$\begin{aligned} &p_n(x) = f[x_0] + f[x_0, x_1] \cdot (x - x_0) + f[x_0, x_1, x_2] \cdot (x - x_0) \cdot (x - x_1) + \\ &... + f[x_0, x_1, ...x_n] \cdot (x - x_0) \cdot (x - x_1) ... \cdot (x - x_{n-1}) \end{aligned} \tag{4.18}$$

where $f[x_0..x_k]$ is, for $k = 0...n$, the element (k,k) of matrix A diagonal:

$$A = \begin{vmatrix} f(x_0) & & & & \\ f(x_1) & \frac{(f(x_1)-f(x_0)}{(x_1-x_0)} & & & \\ f(x_2) & \frac{(f(x_2)-f(x_1)}{(x_2-x_1)} & \frac{A[2,1]-f[x_0,x_1]}{(x_2-x_0)} & & \\ ... & ... & ... & ... & \\ f(x_n) & .. & ... & \frac{(A[n-1,n-2]-A[n,n-2]}{(x_n-x_{n-1})} & \frac{A[n,n-1]-f[x_0,..,x_n]}{(x_n-x_0)} \end{vmatrix} \tag{4.19}$$

It is a interpolation polynomial on the ties x_0, x_1,..x_n, which can be written in recursive form:

$$p_{k+1}(x) = p_k(x) + f[x_0, x_1, ...x_{k+1}] \cdot (x - x_0) \cdot (x - x_1)... \cdot (x - x_{k+1}) \tag{4.20}$$

where $p_k(x)$ is the interpolation polynomial of degree k on ties x_0, x_1,..x_k. The ties x_0, x_1,..x_k are the state vector time and the $f(x_0)$, $f(x_1)$,..$f(x_{k)}$ the state vector position to define satellite flight path and the state vector velocity to calculate the satellite velocity.

4.3.2 The full stereo functional model

The functional model (for example, [28]), in short form, reads: $f(x, y) = 0$. The two equation (Equation 4.30) are written for each available Ground Points (GPs), two for the first image and two for the second image, so we have four equation. The system is not linear and it must be linearized in the form of $Ax + b = 0$.

As usual the solution is obtained for each GPs iteratively due to non-linearity of the system; the iterative procedure stops when the estimated variance of unit weight reaches a local minimum.

d is the **known vector:**

$$d = \begin{vmatrix} d_1 \\ d_2 \end{vmatrix} \rightarrow for\ i^{th}\ GP \begin{cases} d_1^{(i)} = \begin{vmatrix} \tilde{F}_1 \\ \tilde{F}_2 \end{vmatrix} \\ d_2^{(i)} = \begin{vmatrix} \tilde{F}_3 \\ \tilde{F}_4 \end{vmatrix} \end{cases} \tag{4.21}$$

A is the **design matrix:**

$$\mathbf{A} = \left| \begin{array}{c} \mathbf{A}_1^{(i)} \\ \mathbf{A}_2^{(i)} \end{array} \right|$$

$$for\ i^{th}\quad GP \rightarrow \begin{cases} \mathbf{A}_1^{(i)} = \left| \begin{array}{ccc} \partial_{X_i} F_1 & \partial_{Y_i} F_1 & \partial_{Z_i} F_1 \\ \partial_{X_i} F_2 & \partial_{Y_i} F_2 & \partial_{Z_i} F_2 \end{array} \right| \\ \mathbf{A}_2^{(i)} = \left| \begin{array}{ccc} \partial_{X_i} F_3 & \partial_{Y_i} F_3 & \partial_{Z_i} F_3 \\ \partial_{X_i} F_4 & \partial_{Y_i} F_4 & \partial_{Z_i} F_4 \end{array} \right| \end{cases} \tag{4.22}$$

where F_1, F_2, F_3 and F_4 are the model function 4.30 write for the two images.

4.4 Rational Polynomial Functions

The Rational Polynomial Functions (RPFs) model is a well-known method to orientate optical satellite imagery. It is well-known that the RPFs model relates the object point coordinates (latitude ϕ , longitude λ and height h) to the pixel coordinates (I, J) in the form of ratios of polynomial expressions [] whose coefficients (RPCs) are often supplied together with imagery:

$$I = \frac{P_1(\phi, \lambda, h)}{P_2(\phi, \lambda, h)} J = \frac{P_3(\phi, \lambda, h)}{P_4(\phi, \lambda, h)} \tag{4.23}$$

The number of the RPCs obviously depends from the polynomial order (usually limited to the third one), so that each of them takes the generic form:

$$P_n = \sum_{i=0}^{m_1} \sum_{j=0}^{m_2} \sum_{k=0}^{m_3} t_{ijk} \cdot \phi^i \cdot \lambda^j \cdot h^k \tag{4.24}$$

with $0 \leq$ m1 ≤ 3; $0 \leq$ m2 ≤ 3; $0 \leq$ m3 ≤ 3 and m1+m2+m3 ≤ 3 where t_ijk are the RPCs. In case of third order polynomials, the maximum number of coefficients is 80 (20 for each polynomial); actually, it is reduced to 78, since the two equations [4] can be divided for the zero order term of their denominators. The image and ground coordinates in equation are usually normalized to (-1, +1) range in order to improve the numerical accuracy, using the simple formula:

$$T_n = \frac{T - T_{offset}}{T_{scale}} \tag{4.25}$$

where T_n are the normalized coordinates, T_{offset}, T_{scale} are the normalization parameters available in the metadata file and T is the generic original ground or image coordinate ($T = I$, J; ϕ, λ, h).

Overall, the use of the RPFs model is common in several commercial software, at least for three important reasons: a) the implementation of the RPFs model is standard, unique for all the sensors and much more simple that the one of a rigorous model, which has to be customized for each sensor; b) the performance of the RPFs model, using a refinement transformation if needed, can be at the level of the ones from rigorous models; For these reasons, the use of RPCs could be conveniently extended also to SAR imagery. Therefore, considering that only RADARSAT-2 supplies imagery with RPCs file, the RPCs generation tool already implemented in SISAR for optical imagery has been extended to comply with COSMO-SkyMed and TerraSAR-X imagery. RPCs can be generated on the basis of rigorous orientation sensor models.

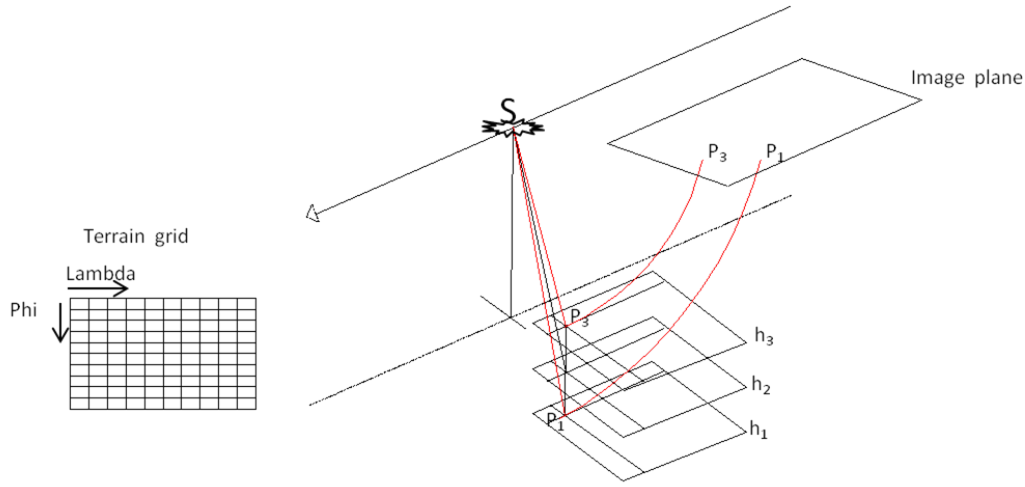

Figure 4.8: RPCs- terrain independent approach

Nevertheless, the first methodology (also called terrain-dependent) is not recommended for two relevant reasons. At first, it is likely to cause large deformations in areas far from the GCPs and it is very weak and vulnerable in presence of outliers. Further, it is not convenient, since the number of required GCPs could

be very high: for example, at least 39 GCPs are necessary if RPCs up to the third order are looked for. In the second methodology, RPCs can be generated according to a terrain-independent scenario, using a known physical sensor model; this is the standard for some sensor managing companies, which supply through imagery metadata a re-parametrized form of the radargrammetric sensor model in term of RPCs, generated from their own secret physical sensor models ([32] and [18]). The developed and implemented procedure to generate RPCs within SISAR is presented hereafter. Three are its main steps: a) at first the image is orientated through the already established radargrammetric orientation model; b) further, 3D object grid with several layers slicing the entire terrain elevation range is generated; the horizontal coordinates of a point of the 3D object grid are calculated from the image corner coordinates with a regular gap, the corresponding (I,J) of the image grid are calculated using the computed orientation model. c) finally, the RPCs are estimated in a least squares solution, having as input the coordinates of the 2D image grid points and of the 3D object grid points.

The coarsest spacing both for 2D and 3D grids definition is dependent on the need to generate enough grid points for the RPCs estimation, considering that each correspondence between a 2D image grid point and a 3D object grid point supplies a couple of linearized RPFs equations:

$$\begin{aligned} &I_n + b_i \cdot \lambda_n \cdot I_n + b_2 \cdot \phi_n \cdot I_n + ... + b_{18} \cdot \phi_n^3 \cdot I_n + b_{19} \cdot h_n^3 \cdot I_n - a_0 - a_1 \cdot \lambda_n - \\ &-a_2 \cdot \phi_n - ... - a_{18} \cdot \phi_n^3 - a_{19} \cdot h_n^3 \\ &J_n + d_i \cdot \lambda_n \cdot J_n + d_2 \cdot \phi_n \cdot J_n + ... + d_{18} \cdot \phi_n^3 \cdot J_n + d_{19} \cdot h_n^3 \cdot J_n - c_0 - c_1 \cdot \lambda_n - \\ &-c_2 \cdot \phi_n ... - c_{18} \cdot \phi_n^3 - c_{19} \cdot h_n^3 \end{aligned} \tag{4.26}$$

where (a_i, b_i, c_i, d_i) are the RPCs to be estimated; on the other hand, there is an incompressible error due to the accuracy of the rigorous model, so that very fine 2D and 3D grid spacings are useless. Since the equations are independent, the least squares estimations are performed separately for the two image coordinates (I_n, J_n) :

$$\begin{aligned} A_I \cdot x_I + y_I = 0 \\ A_J \cdot x_J + y_J = 0 \end{aligned} \tag{4.27}$$

where (A_I, A_J) are the design matrices (including products between image and ground coordinates), (x_I, x_J) are the unknown parameters (RPCs) and (y_I,

y_J) are the known terms (image coordinates); for the first equation we have:

$$A_I = \begin{vmatrix} A_{I,1} \\ A_{I,2} \\ ... \\ A_{I,k} \end{vmatrix} x_I = \begin{vmatrix} a_0 \\ a_1 \\ ... \\ a_19 \\ b_0 \\ b_1 \\ ... \\ b_19 \end{vmatrix} y_I = \begin{vmatrix} In,1 \\ In,2 \\ ... \\ In,k \end{vmatrix} \tag{4.28}$$

with:

$$A_{I,1} = \begin{vmatrix} I_n \cdot \phi_n & I_n \cdot \lambda_n & I_n \cdot h_n & ... & I_n \cdot \phi_n^3 & I_n \cdot \lambda_n^3 & I_n \cdot h_n^3 & -1 & -\phi_n & ... \end{vmatrix} \tag{4.29}$$

and similarly for the second one. Now, it has to be stressed that previous investigations with optical imagery clearly underlined that many RPCs are highly correlated, so that the least squares problem is basically overparametrized; in order to avoid instability due to high correlations, leading to a pseudo-singular design matrix, usually a Tickhonov regularization is adopted, adding a damping factor to the diagonal of the normal matrix. On the contrary, we decided to avoid overparametrization just selecting the actually estimable RPCs (parsimony principle) ([29], [7]).

The Singular Value Decomposition (SVD) and QR decomposition are employed to evaluate the actual rank of the design matrix and to perform this selection; the remaining RPCs need to be constrained to zero[31]. In details, we adopted a SVD-based subset selection procedure due to Golub, Klema and Stewart that proceeds according the main following steps: a) The SVD is computed and used both to calculate the approximate values of RPCs to normalize the design matrix A and to determine its actual rank r; the threshold used to evaluate r is based on the ratio between the maximum and the allowed minimum singular values; reference values are 10-4Ã·10-5 [Press et Al., 1992] b) An independent subset of r columns of A is selected by the QR decomposition with column pivoting: AP=QR. In a system of linear equations (Ax=b), if A has a rank r, the QR decomposition produces the factorization AP=QR where R is:

$$R = Q^T \cdot A \cdot P \tag{4.30}$$

and Q is orthogonal, R_11 is upper triangular and not singular and P is a permutation matrix. At the generic ith step of the QR factorization in the matrix A_i the 2-norm of every column is computed and if the 2-norm of ith column of A_i is longer than the 2-norm of kth column of A_i, the two columns

are interchanged. Consequently the same columns of matrix P are interchanged too. The permutation matrix P is calculated so that the columns of the matrix $B_1 mathcal3 mathfrak R^{mxr}$ in AP=[B_1 B_2] are sufficiently independent; B_1 has a number of columns equal to rank of A. c) B_1 is the matrix extracted from A and used to solve the linearized RPFs equations in the least squares sense, computing the only estimable r RPCs.

Moreover, the statistical significance of each estimable RPC is checked by a Student T-test and the estimation process is repeated until all RPCs are significant. It is important underline that the SAR images are not available with the RPCs in the metadata file, only RADARSAT-2 are supplied with RPCs by head office [8].

Chapter 5

The commercial software PCI-Geomatica

To test the effectiveness of SISAR radargrammetric model and the generally radargrammetry potentialities, the commercial software PCI-Geomatica v. 2012 was been used. The several results computed with the software, were collected at CCRS (Canadian Center of Remote Sensing) in Ottawa (Canada), under the supervision of Prof. Thierry Toutin, who has developed the orientation model implemented in PCI-Geomatica.

5.1 PCI-Geomatica

Geomatica is designed to help analyze and solve the challenging problems we face in our stewardship of the environment, as well as to provide day-to-day support for common GIS and image processing tasks. With the newest release of Geomatica, PCI Geomatics continues to push the boundaries of performance and enable geospatial professionals to solve real-world problems more quickly and cost-effectively [5]. The software include the following tools:

- **Focus**
- **OrthoEngine**
- **Modeler:** PCI Visual Modeler provides an interactive methodology for the development of both simple and complex data processing flows

- **EASI:** Geomatica EASI is a command line interface. The EASI command language can be used to set up and run EASI programs, and write complex procedures

- **FLY!:**Geomatica FLY! is an interactive X/Motif application. It provides near real-time visualization of movement through image data, with an underlying digital elevation model (DEM)

- **SPTA:** SAR Polarimetry Target Analysis (SPTA), which is a key component of the SAR Polarimetry add-on module, is now available from the Geomatica toolbar. The SPTA application lets you select targets within a display of polarimetric SAR (synthetic aperture radar) scene, draw a target (or load an existing one), perform a variety of polarimetry operations on it, and display the results numerically and graphically

- **GeoRaster metadata Mapper:**Through the Oracle Spatial option, the Oracle Database 11g offers the ability to store, index, and manage geographic features represented in raster formats. The GeoRaster Metadata Mapper is a simple tool to help you quickly and efficiently load your raster data sets into your Oracle Spatial database

5.1.1 Focus

Geomatica Focus is a visual environment for working with a variety of data, including imagery, vectors, and graphical bitmaps. It is an application for viewing, enhancing, and examining remotely sensed imagery such as LANDSAT, SPOT, RADARSAT, ERS-1, NOAA AVHRR, Ikonos, and aerial photography. It also enables users to overlay their GIS data and view the attribute information included with such data[5].

In this work, Focus was been used to complementary tool to Radargrammetric DSMs generation from OrthoEngine (pargraph5.1.2). The images were filtered using the Enhanced Lee Filter including in the Focus Algorithm Librarian with different window size. Moreover, the tool was been used to crop the images, to crop and define the over lap areas, to change the coordinate system, actions necessary to DSM extraction. At last, the extract DSMs have been compared with the reference DSM trough Focus Easi Modeling, which give the possibility to write complex procedures. Focus, used for DSMs comparison, give the possibility to see, automatically, the error map, the histogram, to view the current count of pixels for a given pixel value, and the statistics. Moreover, the tool is useful to the classification; it is easy include mask to classify bare surface, no data value, urban area, etc..

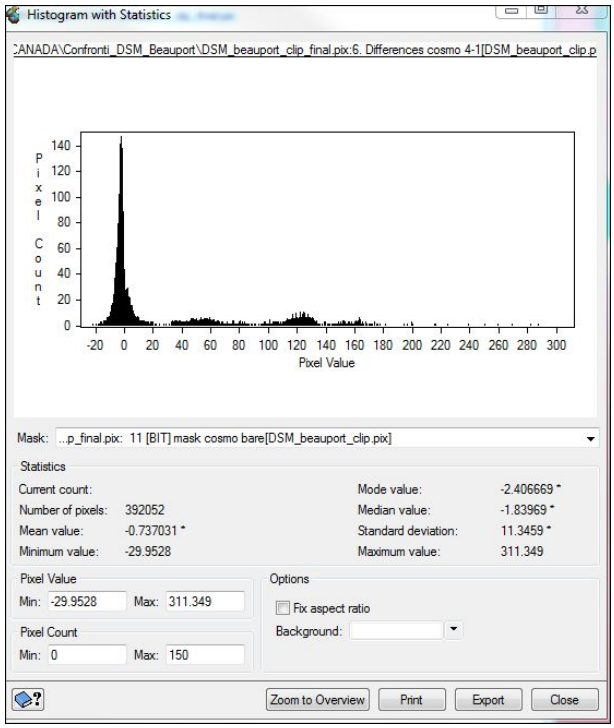

Figure 5.1: Focus Histogram ad statistic windows

5.1.2 OrthoEngine

OrthoEngine is a photogrammetric tool designed to handle production workloads to produce geospatial products [5].

OrthoEngine supports images from standard aerial and SAR and Optical satellite sensors:

In particular SAR sensors included are:

- ASAR - Envisat
- COSMO-SkyMed 1
- COSMO-SkyMed 2

- COSMO-SkyMed 3
- ESRI 1
- ESRI 1
- RADARSAT-1
- RADARSAT-2
- TerraSAR-X

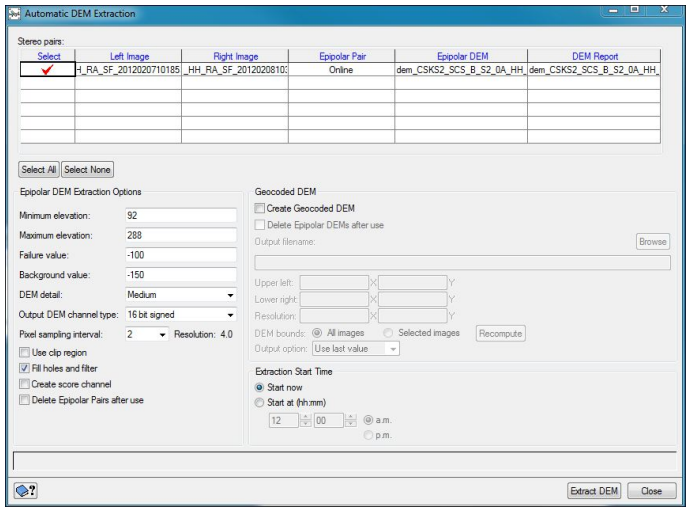

Figure 5.2: Automatic DEM extraction windows

OrthoEngine's interface is organized along logical workflows to produce orthorectified or geometrically corrected images, digital elevation models (DEMs), three-dimensional vectors, and mosaics.

OrthoEngine includes several features for example:

- Rigorous math models which produce robust orthorectification of aerial and satellite imagery.

- Automatic tie point collection
- Epipolar images generation, which converts a group of stereo pairs into epipolar image pairs, useful for automatic DEM and 3-D feature Extraction.
- Automatic DEM Extraction (Fig. 5.2)
- orthorectification or geometrically correction of images

Chapter 6

Analysis and results

IN order to test the effectiveness of the implemented RPCs generation tool and the SISAR radargrammetric orientation model the reference results were computed: the available stereo pairs were orientated with the two model. Moreover, to evaluated the difference accuracy between the orientation model calculated without GCPs and the orientation model calculated with GCPs a Monte Carlo test was computed. At last, the commercial software PCI-Geomatica V. 2012 was used to test the radargrammetry potentialities, under the supervision of Prof. Thierry Toutin that has developed the orientation model implemented in this commercial software.

6.1 Radargrammetric model evaluation: Monte Carlo simulation

In paragraph 4.3.1 it is explain the orbit computation and its contribution in the accuracy orientation; in particular, the two different orbit estimations, the circular arc and the Lagrange polynomials, define the use of GCPs for the stereo image orientation. The first function require the use of GCPs to estimate the metadata parameters corrections while the second one uses the matadata parameters without correct them. To define the GCPs collimation errors and they influences on the accuracy of stereo restitution we use a Monte Carlo simulation. In fact, as is possible see in the Fig. [**?**] the homologous points individuation on radar images is more difficult than on the optical one, and it is possible to

blunder the position. Starting from a no errors configuration, a Gaussian error was applied, with standard deviation 1-6 pixel, to GCPs image coordinates.

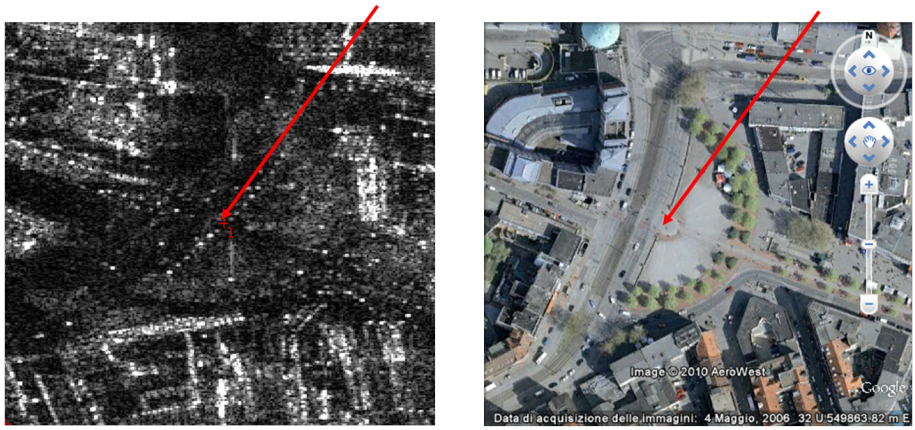

TerraSAR-X Spotlight, SAR image — Google Earth, aerial image

Figure 6.1: Radar collimation

The stereopair was oriented using a different number of GCPs (3,6,9); for each orientation (3,6,9 GCPs) hundred orientation affected by casual errors were computed, at last the orientation accuracy was evaluated computing the RMSE calculated on CPs ground coordinates residuals. The results shown (Tab. 6.1) that the RMSE error due to the collimation on radar image is at level of 1-2 m in horizontal coordinates and 1 m in vertical one, and if the number of GCPs increases the result don't change significantly.

Therefore, the collimation errors have a great relevance on the finally accuracy of stereo restitution, and the possibility of orientated the images without the use of GCPs eliminates this kind of blunders. To shown the comparison between two model, in Table 6.2 are reported the accuracy of a SpotLight COSMO-SkyMed stereo pair orientation obtained with and without the use of GCPs.

The accuracy results of orientation model performed without GCPs are better then the results computed with GCPs.

Coll. err.	RMSE CPs due to collimation errors								
	3 GCPs			6 GCPs			9 GCPs		
St. Dev.	E	N	Up	E	N	Up	E	N	Up
Err. Free	0.00	0.01	0.00	0.00	0.01	0.00	0.00	0.00	0.00
1	0.64	0.35	0.43	0.46	0.26	0.31	0.38	0.20	0.26
2	1.25	0.68	0.84	0.89	0.53	0.59	0.75	0.40	0.50
3	1.93	1.04	1.30	1.40	0.82	0.92	1.12	0.59	0.75
4	2.63	1.36	1.74	1.94	1.08	1.29	1.91	0.78	1.26
5	3.25	1.69	2.16	2.33	1.39	1.54	1.88	1.06	1.26
6	3.78	2.09	2.57	2.72	1.64	1.78	2.32	1.25	1.54

Table 6.1: Monte Carlo simulation

Average CPs [m]			St. Dev CPs [m]			RMSE CPs [m]		
East	North	Up	East	North	Up	East	North	Up
San Pietro island								
No GCPs								
-0.15	0.45	-0.36	2.80	1.94	1.91	2.80	1.99	1.95
3 GCPs								
-1.11	-2.48	0.26	1.89	2.16	2.86	2.19	3.29	2.87

Table 6.2: Difference accuracy with or without GCPs stereo model

6.2 Results COSMO-SkyMed and TerraSAR-X data

6.2.1 Data set

The starting available data for the experiments were COSMO-SkyMed and TerraSAR-X imagery. As regards COSMO-SkyMed (Tab. 6.3): two Spotlight stereo pairs acquired over the area of San Pietro Islands (Italy) (Fig. 6.3)and Merano (North Italy) (Fig. 6.2).

As regards the TerraSAR-X data: three images acquired in High Resolution (HR)SpotLight mode on the Hannover area (Fig. 6.4) and a HR-Spotlight stereo pair acquired on the Trento zone (Fig. 6.5) (Northern Italy). The Hannover imagery arrange two different stereopairs, one same side (ascending) and one op-

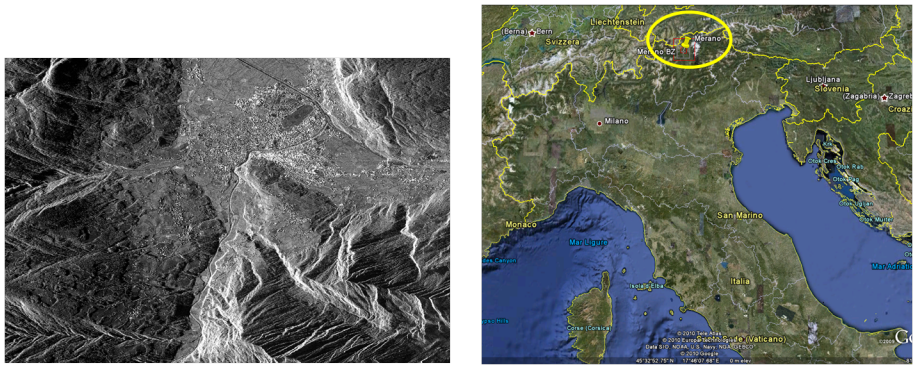

Figure 6.2: Merano test site

Area	Acquisition date	Mean incidence angle (deg)	Orbit	Look side	Acquisition mode
Merano	30/11/2009	25.9	Desc	Right	Spotlight
Merano	02/12/2009	42.3	Desc	Right	Spotlight
San Pietro Island	4/5/2010	48.2	Desc	Right	Spotlight
San Pietro Island	4/5/2010	54.2	Asc	Right	Spotlight

Table 6.3: COSMO-SkyMed images features

posite site (ascending and descending).

All images belongs to the Level 1A (SCS) category products, that is focused data in complex format, in slant range and zero Doppler projection.

The stereo pair accuracy orientation of San Pietro imagery is based on 16 Ground Points (GPs): the GPs have been surveyed by LiDAR tecnology, achieving a vertical accuracy of about 0.25 m. To evaluated the stereo pair orientation of Merano stereo pair we used 20 GPs, of which the horizontal coordinates are derived from cartography (scale 1:5000) whereas the heights come from a LIDAR Digital Terrain Model (mean elevation accuracy of 0.25 m); both these data are free available on the website of the Provincia Autonoma di Bolzano. As regards the Hannover test site, 20 GPs are available, the coordinates were obtained from LiDAR technology, make available in the ISPRS project- Evaluation of DEM derived from TerraSAR-X data. On Trento area, the 13 points used to evaluated

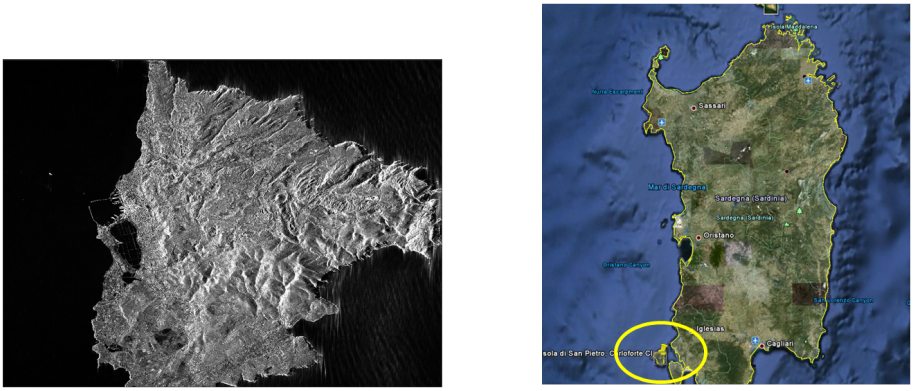

Figure 6.3: San Pietro island test site

Area	Acquisition date	Mean incidence angle (deg)	Orbit	Look side	Acquisition mode
Hannover	05/12/2007	33.8	Asc	Right	HR-Spotlight
Hannover	10/12/2007	44.9	Asc	Right	HR-Spotlight
Hannover	29/12/2007	31.8	Desc	Right	HR-Spotlight
Trento	19/01/2011	24.1	Desc	Right	HR-Spotlight
Trento	14/01/2011	38.9	Desc	Right	HR-Spotlight

Table 6.4: TerraSAR-X images features

Figure 6.4: Hannover test site

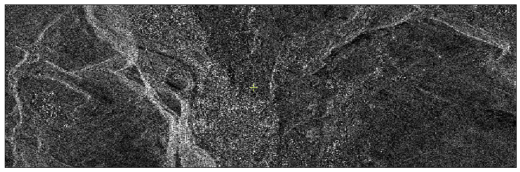

Figure 6.5: Trento test site

the accuracy orientation, came from GPS survey.

6.2.2 Accuracy results of radargrammetric model

At first, it has to be underlined that the result were calculated on the residual on the Control Points (CPs) and the accuracy was evaluated on the RMSE of this CPs residuals.

For Merano stereo pair, the horizontal accuracy is at level of 3.0 - 4.0 m, and the vertical one is around 2.5 m; the average, the standard deviation and the RMSE were shown in Table 6.5 and the accuracy is evaluated in terms of RMSE on CPs residuals (RMSE CPs). For San Pietro test site the stereo pair is opposite side and the results are better then Merano area and are around 2-3 m in horizontal and 2 m in vertical (Tab. 6.5). The opposite side geometry configuration give better results because simplifies the 3D reconstruction and the Doppler rays intersection.

For TerraSAR-X (Tab. 6.6) data the accuracy is similarly to COSMO-SkyMed: for Merano stereo pairs the opposite side images gives better results than same side one, the accuracy is shown in table 6.6, the vertical residuals are around 3 m. The result is the same in the Trento stereo pair orientation.

In conclusion, the stereo restitution accuracy related to COSMO-SkyMed and TerraSAR-X same-side and opposite-side stereo pairs are displayed and this results were obtained without the use of GCPs, a priori ground truth.

Average CPs [m]			St. Dev CPs [m]			RMSE CPs [m]		
East	North	Up	East	North	Up	East	North	Up
San Pietro island								
-0.15	0.45	-0.36	2.80	1.94	1.91	2.80	1.99	1.95
Merano								
1.99	1.10	-0.58	1.99	3.30	2.63	2.81	3.48	2.69

Table 6.5: COSMO-SkyMed radargrammetric model accuracy

Average CPs [m]			St. Dev [m]			RMSE CPs [m]		
East	North	Up	East	North	Up	East	North	Up
Hannover same side								
-0.89	4.46	-0.18	1.60	2.40	2.73	1.83	5.07	2.73
Hannover same side								
-1.83	-0.65	-.216	2.17	2.27	3.14	2.17	2.27	3.14
Trento								
5.78	3.12	3.24	5.78	3.12	3.24	5.89	3.29	3.24

Table 6.6: TerraSAR-X radargrammetric model accuracy

6.2.3 Accuracy results of RPCs model

At first, it has to be underlined that the RPCs were generated on the basis of the mentioned rigorous orientation model, therefore without the use of GCPs. In all these cases, the RPCs generation tool estimated only about 20 coefficients, instead of the 78 coefficients generally employed in the third order RPFs, avoiding the overparametrization and selecting only the estimable and significant parameters as mentioned before. The generated RPCs were used in order to orientate the stereo pairs and the results of RPCs applications are presented in Table 6.7 for COSMO-SkyMed data and in Table 6.8 for TerraSAR-X data: the accuracy level is just close to the one achieved by the rigorous orientation model, what proves the effectiveness of the RPCs generation tool implemented in SISAR.

It was already mentioned that a common drawback of the generalized RPFs model, when the coefficients are estimated according to a terrain-dependent approach, is the high dependence on the actual terrain relief and the inability to reconstruct complex morphologies. On the other hand, RPCs generated according to a terrain-independent approach should provide the sensor orientation, enabling the correct reconstruction of the acquisition geometry and modelling image

Average CPs [m]			St. Dev [m]			RMSE CPs [m]		
East	North	Up	East	North	Up	East	North	Up
San Pietro island								
0.69	-1.16	-0.49	1.86	2.49	2.36	1.99	2.75	2.41
Merano								
0.03	-1.64	1.35	3.42	2.31	2.22	3.42	2.84	2.60

Table 6.7: COSMO-SkyMed RPCs model accuracy

Average CPs [m]			St. Dev [m]			RMSE CPs [m]		
East	North	Up	East	North	Up	East	North	Up
Hannover same side								
0.60	0.61	0.79	2.16	1.96	2.56	2.25	2.05	2.68
Hannover same side								
-0.55	0.12	0.39	2.10	1.69	1.83	2.17	1.69	1.87
Trento								
-1.35	-0.93	0.90	6.13	3.23	3.55	6.28	3.36	3.66

Table 6.8: TerraSAR-X RPCs model accuracy

distortions related to the elevation of the scene.

Our goal is now to show in a simple way that the RPCs generated by the tool implemented in SISAR are able to model the typical SAR distortions in presence of a complex morphology.

To study the effects of the topography, simulation tests were performed. In details, the elevation of a chosen GP has been modified adding different height shifts Δh, and the corresponding image coordinate variations were computed applying the RPCs model (Tab. 6.9). Considering that the column spacing is around 0.4 m, the increase in I coordinates is consistent with the increase in elevation, whereas the line coordinate does not vary significantly, since the GP coordinates are not modified in azimuth direction. These results remark that the generated RPCs model well reflects the physical acquisition of the SAR image even with rough morphology.

AH [m]	I [pix]	J [pix]	AI [pix]
0	6682.3	7272.6	0.0
5	6667.9	7272.6	-14.4
10	6653.5	7272.6	-28.8
50	6538.4	7272.5	-143.9
100	6394.5	7272.3	-287.9
300	5818.7	7271.8	-863.6

Table 6.9: Effect on the image coordinates with respect to the elevation variations as accomplished by the SISAR RPCs model

6.3 Beauport test site results and comparison with OrthoEngine software

In order to test the effectiveness of the implemented SISAR radargrammetric orientation model on the three high resolution SAR satellite data, COSMO-SkyMed, TerraSAR-X and RADARSAT-2, the orientation of three stereopairs acquired on Beuport (Canada) test site, were computed. Moreover, the accuracy of DSMs extracted from OrthoEngine software using radrgrammtric technique and well know Toutin's orientation model, was evaluated.

6.3.1 Beauport Data set

The available data on Beauport (Canada) test site for the experiments were COSMO-SkyMed, TerraSAR-X and RADARSAT-2 imagery. As regards COSMO-SkyMed (Tab. [**?**]) we have a Spotlight stereo pairs acquired in same side mode. Moreover, we have two images acquired by TerraSAR-X sensor in Spotlight mode and two images acquired by RADARSAT-2 in ultrafine mode. All images are in zero Doppler/Slant range projection.

The CSK (COSMO-SkyMed) imagery are supplied by e-Geos whereas the TSX (TerraSAR-X) and R2 (Radrsat-2) images are supplied by CCRS (Canada Centre for Remote Sensing), in particular TSX data are supplied trough DLR (German Aerospace Center). As is possible to show in Tab. 6.10 the three stereo pairs cover different areas, specifically, the R2 images cover a 20X25 KmxKm area with a slow resolution at level of 3X3 mxm, the CSK and TSX images cover a smaller area 10x10 KmxKm with different ground resolution, CSK with a resolution of 1x1 mxm and TSX 2x2 mxm. The overlap area of the three stereo pairs is shown in Fig. 6.7

On the Beauport area a set of 60 Control Points, acquired by GPS survey,

Satellite	Acquisition date	Mean incidence angle (deg)	Orbit	Acquisition mode	Coverage [KmXKm]
R2	14/09/2008	47.9	Desc	Ultrafine	25X20
R2	14/09/2008	31.7	Desc	Ultrafine	25X20
TSX	16/02/2011	28.5	Asc	Spotlight	10X10
TSX	10/02/2011	42.1	Asc	Spotlight	10X10
CSK	07/02/2012	21.4	Asc	Spotlight	10X10
CSK	08/02/2012	45.9	Asc	Spotlight	10X10

Table 6.10: Beauport test site images features

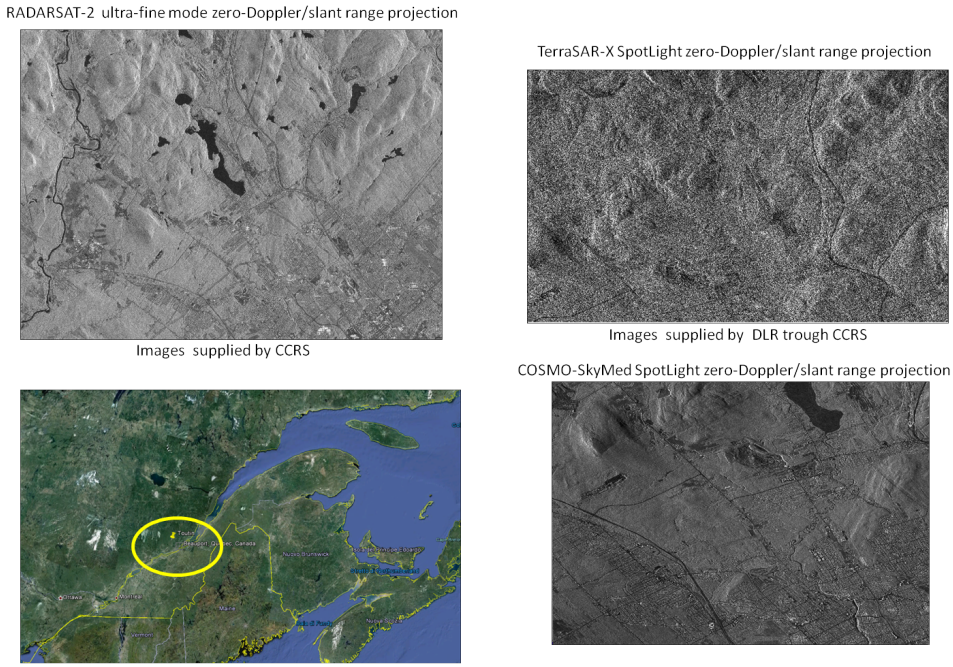

Figure 6.6: Beauport test site

are available and an other set of 20 points was obtained from LiDAR DSM. In fact, the ground truth of the area test is a DSM acquired by LiDAR technology (Fig. 6.8).

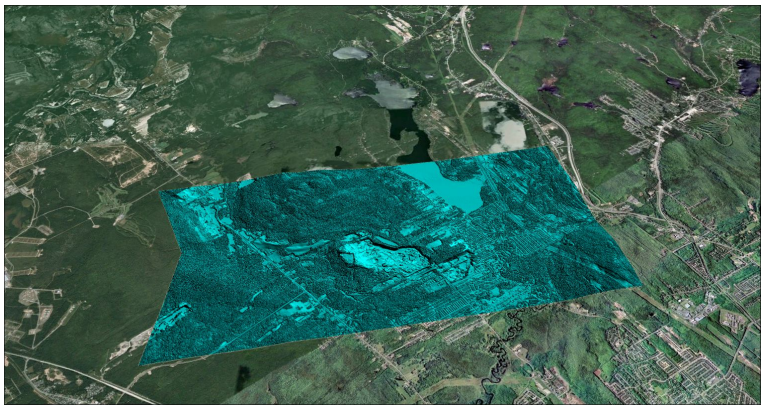

Figure 6.7: Beauport overlap area

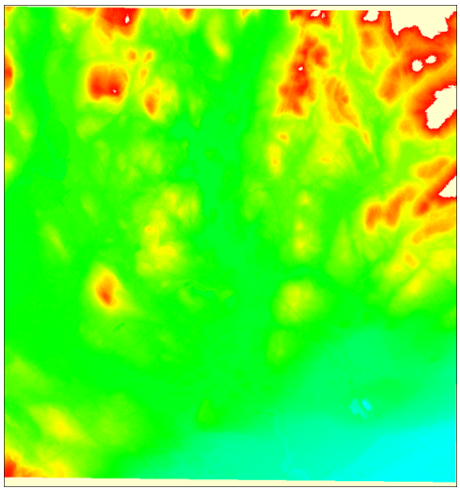

Figure 6.8: LiDAR Beauport area

6.3.2 SISAR model vs Toutin's model: stereo restitution accuracy result on the three high resolution SAR satellite data

At first, it has to be underlined that the result were calculated on the residual on the CPs and the accuracy was evaluated on the RMSE of this CPs residuals. The most important different between the SISAR radargrammetric model and

	Average [m]			St. Dev [m]			RMSE [m]		
	East	North	Up	East	North	Up	East	North	Up
RADARSAT-2									
SISAR	2.71	1.81	-2.29	3.00	1.52	3.08	4.05	2.37	3.83
OE	1.58	1.52	-0.94	0.81	0.86	2.55	1.78	1.75	2.72
TarraSAR-X									
SISAR	-3.83	-1.04	0.64	5.37	3.53	2.52	6.59	3.68	2.60
OE	2.49	3.42	1.32	1.45	2.52	4.53	2.89	4.25	4.72
COSMO-SkyMed									
SISAR	-0.98	2.18	2.40	2.51	2.38	2.00	2.70	3.22	3.13
OE	2.33	2.93	0.83	2.54	3.49	1.64	2.54	3.49	1.64

Table 6.11: Beauport test site model accuracy

the Toutin's model (Paragraph 5.1.2) is the use of GCPs. In fact, the results obtained with OrtoEngine software, in which is implemented the Tountin's model, are computed using a particular set of GCPs. This model needs 12 GCPs to orientate a stereo pairs, this set of points must be have a particular arrangement. In Figure 6.9 is possible see this arrangement, the points are well distributed both in horizontal and in vertical. The results (Tab. 6.11) shown that the Tountin's model accuracy is better than the SISAR model one, overall for COSMO-SkyMed and Radarsat2 data and the difference is about 1 m in up. For TerraSAR-X product, SISAR give better result in up but in East amount at level of 6 m.

.

The SISAR results are good considering the low quality accuracy of available ground points, upon which it was assessed the model accuracy. Moreover, the results of Toutin's model were obtained using 12 GCPs while the SISAR orientation model accuracy is independent of a priori ground truth information.

6.3.3 Radargrammetric DSMs extracted with OrthoEngine

To define the real effectiveness of radargrammetric technique for DSM extraction and to understand the Radrgrammetric tool implementet in a commercial PCI-Geomatica software, we use the images acquired on Beauport test site for DSM extraction by OrthoEngine software. Is important underline that several test were computed. This tests were carried out under the supervision of Prof. Thierry Tountin at CCRS where the PCI-Geomatica orientation model was developed, in order to check the better parameters solution to extract radargrammetric DSMs.

The tests were carried out starting from COSMO-SkyMed data, the result

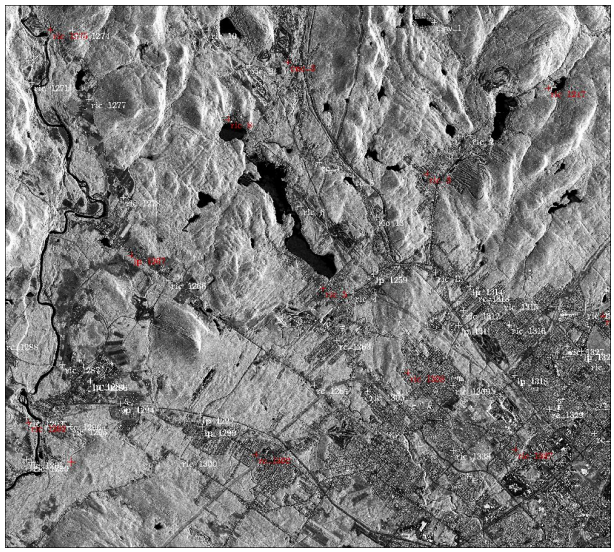

Figure 6.9: GCPs distribution on SAR imagery

are shown in Table 6.12. The images were filtered, before the starting of digital model extraction, in order to reduce the speckle typical of SAR products. The filter used is Enhanced Lee adaptive filter which remove the high frequency noise while preserving high frequency features (edges)[5]. The horizontal filter size used is 13x13 pixel for COSMO-SkyMed data. The size of cross-correlation matching window depend by the relationship between ground resolution and the image resolution, in order to increase the significant statistical number of window pixel.

The second step is the epipolar images generation; OrthoEngine matching algorithm need epipolar or semiepipolar geometry to check the homologous points.

The test were carried out starting from three important OrthoEngine DSM extraction algorithm parameters: *Epipolar downsample*, *details* and *DTM sampling pixel*. The *Epipolar downsample* represents the type the number of image pixels and lines that will be used to calculate one epipolar image pixel. The *details* is the level of detail that you want in the extracted DEM: DEM Detail determines how precisely you want to represent the terrain in the DEM. Selecting High, Medium or Low determines at which point in correlation process you want to stop. Low means that the process stops during the coarse correlation phase on aggregated pixels so the level of detail in the DEM will be quite low. High means the process continues until correlation is performed on images at full resolution [5].

The *DTM sampling pixel* is the number of image pixels and lines (sampling

Epip. Downsam.	Details	DTM Samp. pix	Bias	MIN	MAX	LE90	LE 68
1	High	1	-7.7	-146.7	281.8	-	-
1	Low	2	2.2	-58.3	279.8	84.6	6.9
2	High	2	5.9	-186.0	293.2	10.0	6.2
2	Medium	2	6.0	-185.8	296.7	10.2	6.3
2	Low	2	6.0	-185.2	299.6	10.1	6.4
Bare surface classification							
2	Low	2	0.2	-184.2	288.7	5.09	2.62
DSM merged							
2	H+M+L	2	7.2	-183.8	299.7	10.8	6.5

Table 6.12: Beauport COSMO-SkyMed DSM accuracy

frequency) that will be used to extract one DEM pixel. Using a Pixel Sampling of one pixel is not recommended to derive a DEM for SAR data, because of the difficulties with correlating the speckle inherent in all SAR data. The DSMs accuracy result, in Table 6.12, are evaluated in terms of LE90. For COSMO-SkyMed data the LE90 is at level of 10 m and the LE68 around 6 m. The better resampling for the epipolar images generation is 2 pixel, probably due to the consequently speckle reduce. The classification on bare surface shown that the accuracy reduces at level of 5 m. At last, a test was carried out for COSMO-SKyMed data, the merged of the three DSMs (Low, Medium and High), the results don't increase. In Figure 6.10, the DSMs extracted and the error map are shown. In the red underline zone, where the error is greater, the mountain or urban zone are presented: this zone are affected by typical SAR distortions as Layover and Foreshortening.

For TerraSAR-X product, the steps to extract DSMs were different. The two images were filtered with Lee filter but with a pixel size filter at level of 9x9 pixel. As shown in Table. 6.13 the epipolar images resample at 2 pixel don't increase the final accuracy, probably due to the less TerraSAR-X images resolution then COSMO-SkyMed one. The accuracy is at level of 12 m and the LE68 around 7 m. The same tests were carried out for the bare surface and the result increases and is around 7 m (Tab.6.13).

The red underline zone in Figure 6.11 represent mountain area with a lake, zone affected by Layover and Foreshortening.

As said, the three stereo pairs acquired by the three different sensors cover a small overlap area (Fig.6.7). The RADARSAT-2 imagery are filtered with Lee filter with cross correlation window 13x13 and *epipolar dowsampling* 2 pixel.

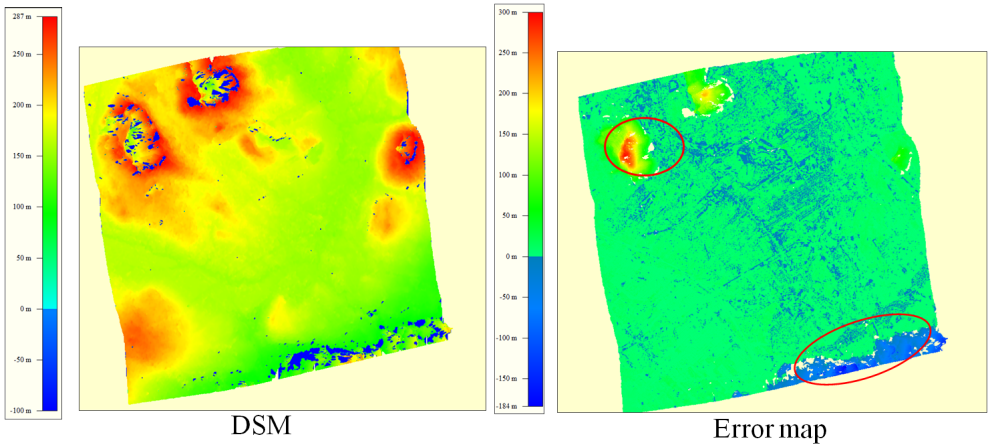

Figure 6.10: DSM COSMO-SkyMed and error map

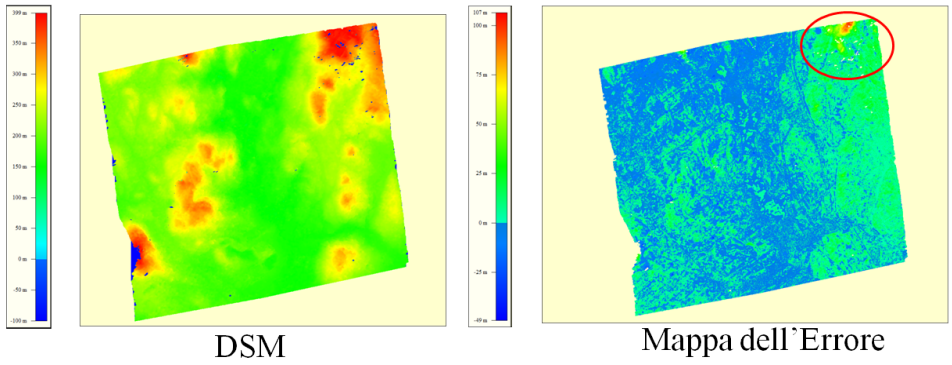

Figure 6.11: DSM TerraSAR-X and error map

In this zone characterized by building area the accuracy result are the same for the COSMO-SkyMed, TerraSAR-X and Radrasat2 data and is at level of 10 m, the results are better on the bare surface than the whole overlap area (Tab. 6.14). In particular, COSMO-SkyMed and TerraSAR-X data give the LE90 value around 5 m, while Radarsat2 accuracy (LE90) is at level of 7 m on bare surface. In this error map tile (Fig. 6.12) it is possible noted the zone with greater error, the building areas: the radargrammetric technique does not reconstruct the urban textures, characterized by typical SAR distortions.

Epip. Downsam.	Details	DTM Samp. pix	Bias	MIN	MAX	LE90	LE 68
1	Low	2	1.4	-49.4	106.5	11.9	6.8
1	Medium	2	1.2	-51.1	104.3	12.2	7
1	High	2	1.5	-53.1	118.6	12.2	7
2	Low	2	0.7	-41	91.4	12	6.4
Bare surface classification							
1	Low	2	-3.4	-45.9	96.9	6.9	3.8
1	Medium	2		-3.5	-51.1	96.6	7.4 4.1
1	High	2	-3.2	-47.5	109.6	7.1	3.9
2	Low	2	-4.3	-37.4	68.3	7.2	4.1

Table 6.13: Beauport TerraSAR-X DSM accuracy

Sensor Downsam.	Epip.	Details Samp. pix	DTM	Bias	MIN	MAX	LE90	LE 68
R2	2	Medium	2	-1.7	-39.9	342.1	10.5	6.0
TSX	1	Low	2	-0.6	-274	274.1	9.6	5.3
CSK	2	Low	2	6.9	-30	373.8	11.6	8.4
Bare surface classification								
R2	2	Medium	2	-5.6	-39.2	216.2	7.3	4.1
TSX	1	Low	2	-4.1	-185	234.3	5.3	2.7
CSK	2	Low	2	-0.7	-30	311.4	4.6	2.5

Table 6.14: Beauport CSK, TSX, R2 comparison - DSM accuracy

6.4 Radargrammetric model: comparison with metadata Tie Points

TerraSAR-X and RADARSAT-2 product have in the metadata a number of Tie Points that give a regular grid. This points were calculated directly by the vendors, using the intrinsic radar geometry acquisition model. This points have image and ground coordinates, so the object coordinates of each point were used in order to determinate the image coordinates with the model implemented in SISAR. The image coordinates residuals shown that the defined and implemented model has a similar behaviour respect the intrinsic SAR acquisition geometry. (Tab. 6.15).

Average CPs [m]		St. Dev [m]		RMSE CPs [m]	
I[pix]	J [pix]	I[pix]	J [pix]	I[pix]	J [pix]
RADARSAT-2 Beuaport 14/09/2008					
-0.01	0.02	0.01	0.02	0.02	0.03
RADARSAT-2 Beuaport 10/09/2008					
-0.02	-0.01	0.04	0.02	0.04	0.03
TerraSAR-X Beuaport 16/02/2011					
0.57	0.83	0.29	0.28	0.64	0.87
TerraSAR-X Beuaport 10/02/2011					
0.50	0.69	0.30	0.15	0.58	0.71
TerraSAR-X Hannover 5/12/2007					
0.25	0.32	0.28	0.26	0.38	0.41
TerraSAR-X Hannover 10/12/2007					
0.31	0.39	0.29	0.29	0.43	0.49
TerraSAR-X Hannover 29/12/2007					
0.47	0.40	0.30	0.28	0.55	0.48
TerraSAR-X Trento 19/01/2011					
0.30	0.41	0.3	0.31	0.42	0.52
TerraSAR-X Trento 14/01/2011					
-0.50	0.27	0.30	0.58	0.58	0.39

Table 6.15: Accuracy result on metadata Tie Points

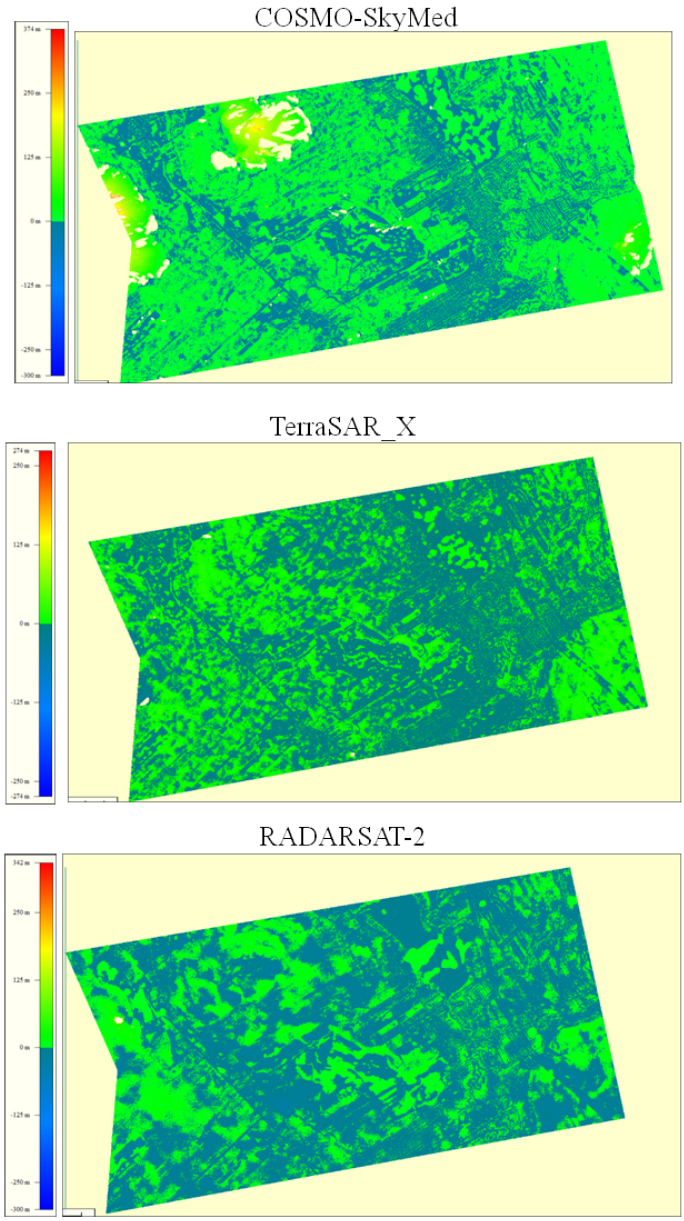

Figure 6.12: CSK, TSX and R2 DSM error map

Chapter 7

Conclusions

The purpose of this work was the definition and implementation of a new model for the orientation of stereo pairs collected by high resolution SAR satellite with the aim of supporting the radargrammetric generation of Digital Surface Models. The model has been implemented in SISAR software, developed at Geodesy and Geomatic Institute of the University of Rome "La Sapienza". Several tests were carried out in order to evaluate the level accuracy of 3D reconstruction. At first, the SISAR model oriented SAR images using few number of GCPs, subsequently, by modifying orbit interpolation, the software allowed the possibility to orientate stereo pair without using ground truth. At first, in order to evaluate the difference accuracy between the orientation model calculated without GCPs and the orientation model calculated with GCPs and the influences of GCPs collection on SAR images to the finally accuracy of stereo model, some tests were computed. In particular several stereo pairs were oriented with and without the use of GCPs. The results shown that the final accuracy is better for the stereo model computed without GCPs. Moreover, to define the influences of GCPs collected on SAR imagery, a Montecarlo test was computed. The CPs RMSE error due to the collimation on radar image is at level of 1-2 m in horizontal coordinates and 1 m in vertical one, and if the number of GCPs increases, the results don't change significantly. Therefore, the collimation error has a great relevance on the final accuracy of stereo restitution, and the possibility of orientating the images without the use of GCPs removes this kind of blunders. The first available SAR data were the COSMO-SkyMed and TerraSAR-X SpotLight stereo pairs, acquired on Merano (same side configuration) and San Pietro is-

land (opposite side configuration) test site and Hannover (opposite and same side configuration) and Trento (same side configuration) zone respectively.

The COSMO-SkyMed accuracy evaluation shows that the vertical accuracy is about 2/3 m and is better for the stereo pair in opposite side configuration. For TerraSAR-X data the accuracy is similar to COSMO-SkyMed: for Merano steropairs the opposite side images provides better results than same side one, the vertical residuals are around 3 m as for Trento images.

Moreover a tool for the RPCs generation suited to SAR imagery has been included in SISAR software. The application of RPCs model to SAR stereo pairs provides good results, comparable with those derived through the radargrammetric rigorous model, what proves the effectiveness of the RPCs generation tool implemented in SISAR.

The results obtained are representative of the geometric potentialities of Spot-Light stereo pairs as regards 3D surface reconstruction. Anyway, it has to be recalled that the accuracy of the DSMs generated by the radargrammetric approach is strictly affected by the quality of the subsequent matching procedure. The radargrammetric approach developed is promising, especially considering that this results were obtained without the use of GCPs, a priori ground truth.

Moreover,in order to test the effectiveness of the implemented SISAR radargrammetric orientation model on the three high resolution SAR satellite data, COSMO-SkyMed, TerraSAR-X and RADARSAT-2, the orientation of three stereo pairs acquired on Beuport (Canada) test site, were computed. A test to compare the SISAR model and the well know Toutin's model implemented in PCI-Geomatica was carried out.

The result shown that the Tountin's model accuracy is slightly better than the SISAR model one, but the SISAR results are good considering the low quality accuracy of available ground points, upon which it was assessed the model accuracy. Moreover, the results of Toutin's model were obtained using 12 GCPs while the SISAR orientation model accuracy is independent of a priori ground truth information.

To define the real effectiveness of radargrammetric technique for DSM extraction and to understand the radargrammetric tool implemented in a commercial PCI-Geomatica software, the images acquired on Beauport test site for DSM extraction by OrthoEngine software has been used. It is important to underline that several test were computed. These tests were carried out under the supervision of Prof. Thierry Tountin at CCRS where the PCI-Geomatica orientation model was developed, in order to check the better parameters solution to extract radargrammetric DSMs. The DSM extracted, using OrthoEngine, shown the advantages and potentiality of radargrammetric technique as alternative or complementary solution to the interferometric technique in order to generated digital model from SAR data. These results should be compared with the com-

plete radargrammetric tool for DSM generation from SAR data implemented in SISAR [24], in order to define the different accuracy between the DSMs extracted using OrtoEngine and SISAR software.

At last, the accuracy computed on metadata Tie Points available in TerraSAR-X and RADARSAT-2 product at level of sub pixel proves that the SISAR model has a similar behaviour respect the intrinsic SAR acquisition geometry

Based on the achieved results, the defined and implemented model results a very suitable and reliable tool for orienting stereo pairs images acquired by COSMO-SkyMed, TerraSAR-X and RADARSAT-2 satellites.

However, further test should be performed both on Stripmap images and on data acquired by new SAR satellite sensor, as Sentinel-1, a ESA (European Space Agency) C band imaging radar mission to provide imagery for GMES (Global Monitoring for Environment and Security) user services.

Acknowledgements

Part of the research activities on this thesis was carried out at CCRS (Canada Centre for Remote Sensing). I would like to express a special thank to Prof. Thierry Toutin, who led me throughout this experience. The author is indebted to e-Geos, DLR and CCRS for making available the SAR images, which have been used for the tests.

Ringraziamenti

In italiano ringrazieró tutte le persone che hanno avuto a cuore e hanno seguito questo mio percorso di ricerca, da vicino e da lontano.

I miei primi ringraziamenti vanno al Prof. Mattia Crespi, che ha seguito la mia attivitá di ricerca con entusiasmo e curiositá scientifica mostrandosi sempre una grandissima fonte di insegnamento.

Grazie a FraP e Andrea con i quali ho condiviso questi tre anni tra confronti, scontri, chiacchiere e allegria, sono stati dei preziosissimi compagni di viaggio, porteró sempre con me il ricordo delle merende canadesi di Francesca e le lezioni filosofiche sul pesce palla di Andrea.

Un pensiero particolare va a Alberico, per aver corretto le bozze di questa tesi e per aver sempre riservato la sedia a fianco delle sua scrivania per me.

Ringrazio tutti i lavoratori della ricerca di quest'area, tutti i ragazzi con cui ho trascorso questi tre anni, un grazie a Elisa, Mara, Augusto, Grabriele, FraF, FraG, Silvia, Martina, Martina, Vittoria, un grazie per tante cóse a Marianna e al mio compare Peppe. Insomma Grazie a tutti i precari perché il nostro é un lavoro che vale.

Bibliography

[1] *Canadian Space Agency - RADARSAT-2 Resolution, polarization and imaging - Available at: http://www.asc-csa.gc.ca/eng/default.asp*, 2007.

[2] *Italian Space Agency - COSMO-SkyMed SAR Products Handbook - Available at https://eopi.asi.it*, 2007.

[3] *Italian Space Agency - COSMO-SkyMed System Description and User Guide - Available at https://eopi.asi.it*, 2007.

[4] *Infoterra - Terra SAR-X Services Image Product Guide - Available at: http://www.infoterra.de/documents*, 2009.

[5] PCI Geomatics - PCI Geomatica 2012 User Guide.

[6] *ESA - ASAR Products Handbook - Available at: https://earth.esa.int/handbooks/asar/CNTR1-1-2.htm*, 2013.

[7] Box, M., Jenkins, M., Reinsel, F., and F. Time Series Analysis-Forecasting and Control. *Prentice Hall*.

[8] Capaldo, P., Crespi, M., Fratarcangeli, F., Nascetti, A., and Pieralice, F. A radargrammetric orientation model and a RPCs generation tool for COSMO-SkyMed and TerraSAR-X High Resolution SAR. *Italian Journal of Remote Sensing 44*.

[9] Capaldo, P., Crespi, M., Fratarcangeli, F., Nascetti, A., and Pieralice, F. High resolution SAR imagery. Radargrammetric application with COSMO-SkyMed. *IEEE Geoscience and Remote Sensing Letters 8*.

[10] Capaldo, P., Crespi, M., Fratarcangeli, F., Nascetti, A., and Pieralice, F. Radargrammetric Digital Surface Models generation from TerraSAR-X imagery: case studies, problems and potentialities. *Photogrammetry, Remote Sensing and Spatial Information Sciences XXXIX-B7*.

[11] Crespi, M., Fratarcangeli, F., Giannone, F., Jacobsen, K., and Pieralice, F. Orientation of Cartosat-1 Stereo Imagery. *Proceeding of EARSeL Joint Workshop Remote Sensing, New Challenges of High Resolution* (2008).

[12] Crespi, M., Fratarcangeli, F., Giannone, F., and Pieralice, F. A new rigorous model for High Resolution Satellite Imagery orientation: application to EROS A and QuickBird. *International Journal of Remote Sensing (in press)* (2010).

[13] Ei-Sheimy, N., Valeo, C., and Habib, A. Digital Terrein Modeling. *Artech House* (2005).

[14] Fayard, F., Meric, S., and Pottier, E. Matching stereoscopic SAR images for radargrammetric applications. *International Geoscience and Remote Sensing Symposium, Barcelona (Spain)* (2007).

[15] Frost, V., Stiles, J., Shanmugan, K., and Holtzman, J. A model for radar images and its application to adaptive digital filtering of multiplicative noise. *IEEE Transaction on Pattern Analysis and Machine Intelligence PAMI-4*, 2 (1982), 157–166.

[16] Gruen, A., Zhang, L., and Kocaman, S. High Accuracy 3D Processing of Satellite Imagery. *Proceeding of JACIE Civil Commercial Imagery Evaluation Workshop* (2006).

[17] Hadjitheophanous, S., Ttofis, C., Georghiades, A. S., and Theocharides, T. Towards Hardware Stereoscopic 3D Reconstruction . *Cyprus Research Promotion Foundation* (2010).

[18] Hanley, H., and Fraser, C. S. Sensor orientation for high-resolution satellite imagery: further insights into bias-compensated RPC. *Proceeding of XX ISPRS Congress, Istanbul, Turkey* (2004).

[19] Lanari, R., S.Zoffoli, Sansosti, E., Fornaro, G., and Serafino, F. New approach for hybrid strip-map/spotlight SAR data focusing. *Radar, Sonar and Navigation, IEE Proceedings 148* (2001), 363–372.

[20] Leberl, F. W. Radargrammetric image processing. *Artec House, Norwood MA* (1990).

[21] Lee, J. Refined filtering of image noise using local statistics. *Computer graphics and Image Processing* (1981), 380–389.

[22] Mansourpour, M., Rajabi, M., and Blais, J. A. R. Effects and performance of speckle noise reduction filters on active radar and SAR images. *ISPRS Workshop, Topographic Mapping from Space, Ankara (Turkey)* (2006).

[23] Meric, S., Fayard, F., and Pottier, E. Radargrammetric SAR image processing. *In: Pei-Gee Peter Ho (Eds.), Geoscience and Remote Sensing, Intech* (2009), 421–454.

[24] Nascetti, A. High resolution radargrammetry: development and implementation of an innovative image matching strategy, 2013. PhD Thesis - Supervisor: Crespi M.

[25] Pieralice, F. A radargrammetric orientation model for sar high resolution imagery, 2011. PhD Thesis - Supervisor: Crespi M.
Available online at: http://padis.uniroma1.it/handle/10805/1276.

[26] Prade, G. L. An Analytical and Experimental Study of Stereo for Radar. *Photogrammetric Engineering 29(2)* (1963), 294–300.

[27] Raggam, H., Gutjahr, K., Perko, R., and Schardt, M. Assessment of the Stereo-Radargrammetric Mapping Potential of TerraSAR-X Multibeam Spotlight Data. *IEEE Transactions on Geoscience and Remote Sensing 48*, 2 (2010).

[28] Sansò, F. Il trattamento statistico dei dati. *Editore CLUP, Milano* (1989).

[29] Sansò, F., Dermanis, A., and Gruen, A. An overview of data analysis methods in geomatics. . *Geomatic methods for the analysis of data in the earth sciences, Springer* (2000).

[30] Shi, Z., and Fung, K. A comparison of digital speckle filters. *Geoscience and Remote Sensing Symposium, 1994. Surface and Atmospheric Remote Sensing: Technologies, Data Analysis and Interpretation 4* (1994), 2129–2133.

[31] Strang, G., and Borre, K. *Linear Algebra, Geodesy and GPS*. 1997.

[32] Tao, C., and Hu, Y. The rational function model. A tool for processing high resolution imagery. *Earth Observation Magazine 10*, 1 (2001), 13–16.

[33] Teunissen, P., and Kleusberg, A. GPS for Geodesy. *Springer-Verlag. ISBN: 3-540-63661-7* (1998).

[34] Toutin, T. Stereo RADARSAT for Mapping Applications. *2nd International ADRO Symposium, Montreal, Canada* (1998).

[35] Toutin, T., and Chenier, R. 3-D radargrammetric modeling of RADARSAT-2 Ultrafine Mode: preliminary results of the geometric calibration. *IEEE Geoscience and Remote Sensing Letters 6*, 2 (2009).

[36] Toutin, T., and Gray, L. State-of-the-art of elevation extraction from satellite SAR data. *ISPRS Journal of Photogrammtery & Remote Sensing 55* (2000), 13–33.

[37] Wegner, J. D., Auer, S., and Soergel, U. Extraction and geometrical accuracy of Double-bounce lines in high resolution SAR images. *Photogrammetric Engineering and Remote Sensing 76*, 9 (2010), 1071–1080.

[38] Wellenhof, B. H., Lichtenegger, H., and Wasle, E. GNSS Global Navigation Satellite System. *Spinger-Verlag. ISBN: 978-3-211-73012-6* (2008).